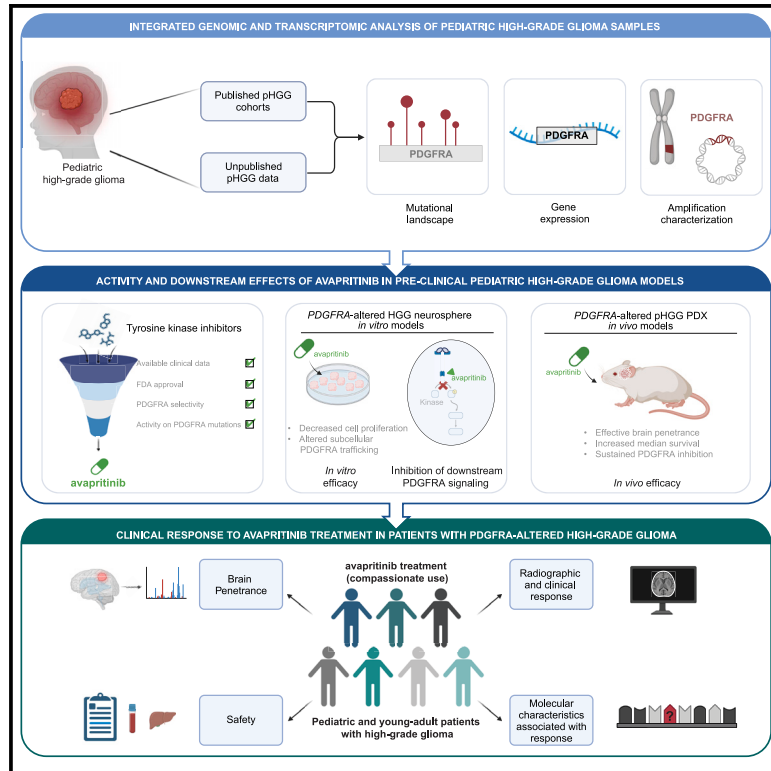


# Effective targeting of PDGFRA-altered high-grade glioma with avapritinib

## Graphical abstract



## Authors

Lisa Mayr, Sina Neyazi, Kallen Schwark, ..., Carl Koschmann, Johannes Gojo, Mariella G. Filbin

## Correspondence

ckoschma@med.umich.edu (C.K.), johannes.gojo@meduniwien.ac.at (J.G.), mariella.filbin@childrens.harvard.edu (M.G.F.)

## In brief

PDGFRA is commonly altered in pediatric HGG. Mayr et al. report that the PDGFRA/KIT inhibitor avapritinib demonstrates on-target activity, brain penetration, and survival benefit in pre-clinical H3K27M DMG models. In pediatric HGG patients, avapritinib treatment is well tolerated and results in radiographic and clinical response in a subset of patients.

## Highlights

- Avapritinib effectively and selectively inhibits PDGFRA signaling in gliomas
- Avapritinib shows CNS penetration and efficacy in pediatric high-grade glioma models
- Safety profile of avapritinib is favorable in pediatric high-grade glioma patients
- A subset of patients with PDGFRA-altered HGG shows clinical response to avapritinib

Article

# Effective targeting of PDGFRA-altered high-grade glioma with avapritinib

Lisa Mayr,<sup>1,2,41</sup> Sina Neyazi,<sup>1,41</sup> Kallen Schwark,<sup>3,41</sup> Maria Trissal,<sup>1,41</sup> Alexander Beck,<sup>4</sup> Jenna Labelle,<sup>1</sup> Sebastian K. Eder,<sup>1,5</sup> Liesa Weiler-Wichtl,<sup>2</sup> Joana G. Marques,<sup>1</sup> Carlos A.O. de Biagi-Junior,<sup>1</sup> Costanza Lo Cascio,<sup>1</sup> Owen Chapman,<sup>6</sup> Sunita Sridhar,<sup>6</sup> Rishaan Kenkre,<sup>6</sup> Aditi Dutta,<sup>6</sup> Shanqing Wang,<sup>6</sup> Jessica Wang,<sup>6</sup> Olivia Hack,<sup>1</sup> Andrezza Nascimento,<sup>1</sup> Cuong M. Nguyen,<sup>1</sup> Sophia Castellani,<sup>1</sup> Jacob S. Rozowsky,<sup>1</sup>

(Author list continued on next page)

<sup>1</sup>Department of Pediatric Oncology, Dana-Farber/Boston Children's Cancer and Blood Disorder Center and Harvard Medical School, Boston, MA 02215, USA

<sup>2</sup>Department of Pediatrics and Adolescent Medicine, Comprehensive Center for Pediatrics and Comprehensive Cancer Center, Medical University of Vienna, 1090 Vienna, Austria

<sup>3</sup>Department of Pediatrics, University of Michigan Medical School, Ann Arbor, MI 48109, USA

<sup>4</sup>Center for Neuropathology and Prion Research, Ludwig Maximilians University Munich, Faculty of Medicine, Muenchen, 80539 Bayern, Germany

<sup>5</sup>St. Anna Children's Hospital, Department of Pediatrics and Adolescent Medicine, Medical University of Vienna and St. Anna Children's Cancer Research Institute (CCRI), 1090 Vienna, Austria

<sup>6</sup>Sanford Burnham Prebys Medical Discovery Institute, San Diego, CA 92037, USA

<sup>7</sup>Department of Neurosurgery, Comprehensive Center for Pediatrics and Comprehensive Cancer Center, Medical University of Vienna, 1090 Vienna, Austria

<sup>8</sup>Center for Cancer Research and Comprehensive Cancer Center, Medical University of Vienna, 1090 Vienna, Austria

<sup>9</sup>Research Cluster "Translational Cancer Therapy Research", University of Vienna and Medical University of Vienna, 1090 Vienna, Austria

<sup>10</sup>Department of Medicine, Massachusetts General Hospital, Boston, MA 02114, USA

<sup>11</sup>Institute for Analytical and General Chemistry, Johannes Kepler University, 4040 Linz, Austria

<sup>12</sup>Central European Institute of Technology, Masaryk University, 60177 Brno, Czech Republic

<sup>13</sup>Department of Experimental Biology, Faculty of Science, Masaryk University, 61137 Brno, Czech Republic

<sup>14</sup>International Clinical Research Center, St. Anne's University Hospital, Brno, Czech Republic

<sup>15</sup>Department of Radiotherapy, Medical University of Vienna, 1090 Vienna, Austria

<sup>16</sup>Department of Biology, Faculty of Medicine, Masaryk University, 62500 Brno, Czech Republic

<sup>17</sup>Lurie Family Imaging Center, Center for Biomedical Imaging in Oncology, Dana-Farber Cancer Institute, Boston, MA 02210, USA

(Affiliations continued on next page)

## SUMMARY

PDGFRA is crucial to tumorigenesis and frequently genomically altered in high-grade glioma (HGG). In a comprehensive dataset of pediatric HGG ( $n = 261$ ), we detect PDGFRA mutations and/or amplifications in 15% of cases, suggesting PDGFRA as a therapeutic target. We reveal that the PDGFRA/KIT inhibitor avapritinib shows (1) selectivity for PDGFRA inhibition, (2) distinct patterns of subcellular effects, (3) *in vitro* and *in vivo* activity in patient-derived HGG models, and (4) effective blood-brain barrier penetration in mice and humans. Furthermore, we report preliminary clinical real-world experience using avapritinib in pediatric and young adult patients with predominantly recurrent/refractory PDGFRA-altered HGG ( $n = 8$ ). Our early data demonstrate that avapritinib is well tolerated and results in radiographic response in 3/7 cases, suggesting a potential role for avapritinib in the treatment of HGG with specific PDGFRA alterations. Overall, these translational results underscore the therapeutic potential of PDGFRA inhibition with avapritinib in HGG.

## INTRODUCTION

Brain tumors remain the leading cause of cancer-related death in childhood. In particular, pediatric high-grade gliomas (pHGGs), including H3K27M diffuse midline gliomas (DMGs), are a fatal group of diseases with a median survival of less

than 18 months after diagnosis.<sup>1–4</sup> Platelet-derived growth factor receptor alpha (PDGFRA) is implicated in the pathogenesis of high-grade glioma on multiple levels. First, genomic PDGFRA alterations, specifically amplifications and/or activating point mutations, have been commonly reported in pHGG and adult glioblastoma (GBM).<sup>5–8</sup> Second, PDGFRA

Andrew Groves,<sup>1</sup> Eshini Panditharatna,<sup>1</sup> Gustavo Alencastro Veiga Cruzeiro,<sup>1</sup> Rebecca D. Haase,<sup>1</sup> Kuscha Tabatabai,<sup>1</sup> Sibylle Madlener,<sup>2</sup> Jack Wadden,<sup>3</sup> Tiffany Adam,<sup>3</sup> Seongbae Kong,<sup>3</sup> Madeline Miclea,<sup>3</sup> Tirth Patel,<sup>3</sup> Katharina Bruckner,<sup>2,7</sup> Daniel Senfter,<sup>2</sup> Anna Lämmerer,<sup>2,8,9</sup> Jeffrey Supko,<sup>10</sup> Armin S. Guntner,<sup>11</sup> Hana Palova,<sup>12</sup> Jakub Neradil,<sup>13,14</sup> Natalia Stepien,<sup>2</sup> Daniela Lötsch-Gojo,<sup>7</sup> Walter Berger,<sup>8,9</sup> Ulrike Leiss,<sup>2</sup> Verena Rosenmayr,<sup>2</sup> Christian Dorfer,<sup>7</sup> Karin Dieckmann,<sup>15</sup> Andreas Peyrl,<sup>2</sup> Amedeo A. Azizi,<sup>2</sup> Alicia Baumgartner,<sup>1,2</sup> Ondrej Slaby,<sup>12,16</sup> Petra Pokorna,<sup>12</sup> Louise M. Clark,<sup>17</sup> Amy Cameron,<sup>17</sup> Quang-De Nguyen,<sup>17</sup> Hiroaki Wakimoto,<sup>18</sup> Frank Dubois,<sup>1</sup> Noah F. Greenwald,<sup>19,20</sup> Prati Bandopadhyay,<sup>1</sup> Rameen Beroukhi,<sup>19,21</sup> Keith Ligon,<sup>1</sup> Christof Kramm,<sup>22</sup> Annika Bronsema,<sup>23</sup> Simon Bailey,<sup>24,25</sup> Ana Guerreiro Stucklin,<sup>26</sup> Sabine Mueller,<sup>27</sup> Mary Skrypek,<sup>28</sup> Nina Martinez,<sup>29</sup> Daniel C. Bowers,<sup>30</sup> David T.W. Jones,<sup>31,32</sup> Chris Jones,<sup>33</sup> Natalie Jäger,<sup>34</sup> Jaroslav Sterba,<sup>35</sup> Leonhard Müllauer,<sup>36</sup> Christine Haberler,<sup>37</sup> Chandan Kumar-Sinha,<sup>38</sup> Arul Chinnaiyan,<sup>38</sup> Rajen Mody,<sup>3</sup> Lukas Chavez,<sup>6</sup> Julia Furtner,<sup>39,40</sup> Carl Koschmann,<sup>3,41,\*</sup> Johannes Gojo,<sup>2,41,\*</sup> and Mariella G. Filbin<sup>1,19,41,42,\*</sup>

<sup>18</sup>Department of Neurosurgery, Massachusetts General Hospital, Harvard Medical School, Boston, MA 02114, USA

<sup>19</sup>Broad Institute of MIT and Harvard, Cambridge, MA 02142, USA

<sup>20</sup>Department of Cancer Biology, Dana-Farber/Boston Children's Cancer and Blood Disorder Center and Harvard Medical School, Boston, MA 02115, USA

<sup>21</sup>Department of Cancer Biology and Medical Oncology, Dana-Farber Cancer Institute, and Harvard Medical School, Boston, MA 02115, USA

<sup>22</sup>Division of Pediatric Hematology and Oncology, University Medical Center Göttingen, 37099 Göttingen, Germany

<sup>23</sup>Clinic of Pediatric Hematology and Oncology, University Medical Center Hamburg-Eppendorf, 20251 Hamburg, Germany

<sup>24</sup>Great North Childrens Hospital and Newcastle University, Newcastle upon Tyne, UK

<sup>25</sup>Newcastle Hospitals NHS Foundation Trust, NE1 4LP Newcastle, UK

<sup>26</sup>Department of Oncology and Children's Research Center, University Children's Hospital Zurich, 8008 Zurich, Switzerland

<sup>27</sup>Departments of Pediatrics, Neurology, and Neurological Surgery, University of California San Francisco, San Francisco, CA 94143, USA

<sup>28</sup>Department of Pediatric Hematology-Oncology, Children's Minnesota, Minneapolis, MN 55404, USA

<sup>29</sup>Department of Neurology & Neurological Surgery, Jefferson University, Philadelphia, PA 19107, USA

<sup>30</sup>Department of Pediatrics, University of Texas Southwestern Medical Center, Dallas, TX 75390, USA

<sup>31</sup>Hopp Children's Cancer Center Heidelberg (KITZ), 69120 Heidelberg, Germany

<sup>32</sup>Pediatric Glioma Research Group, German Cancer Research Center (DKFZ), 69120 Heidelberg, Germany

<sup>33</sup>Division of Molecular Pathology, Institute of Cancer Research, SM2 5NG London, UK

<sup>34</sup>Hopp Children's Cancer Center Heidelberg (KITZ) & Division of Pediatric Neurooncology, German Cancer Research Center (DKFZ), 69120 Heidelberg, Germany

<sup>35</sup>Department of Pediatric Oncology, University Hospital Brno and Faculty of Medicine, Masaryk University, 662630 Brno, Czech Republic

<sup>36</sup>Department of Pathology, Medical University of Vienna, 1090 Vienna, Austria

<sup>37</sup>Division of Neuropathology and Neurochemistry, Department of Neurology, Medical University of Vienna, 1090 Vienna, Austria

<sup>38</sup>Department of Pathology, University of Michigan Medical School, Ann Arbor, MI 48109, USA

<sup>39</sup>Division of Neuroradiology and Musculoskeletal Radiology, Department of Biomedical Imaging and Image-Guided Therapy, Medical University of Vienna, 1090 Vienna, Austria

<sup>40</sup>Research Center of Medical Image Analysis and Artificial Intelligence, Danube Private University, 3500 Krems an der Donau, Austria

<sup>41</sup>These authors contributed equally

<sup>42</sup>Lead contact

\*Correspondence: [ckoschma@med.umich.edu](mailto:ckoschma@med.umich.edu) (C.K.), [johannes.gojo@meduniwien.ac.at](mailto:johannes.gojo@meduniwien.ac.at) (J.G.), [mariella.filbin@childrens.harvard.edu](mailto:mariella.filbin@childrens.harvard.edu) (M.G.F.) <https://doi.org/10.1016/j.ccell.2025.02.018>

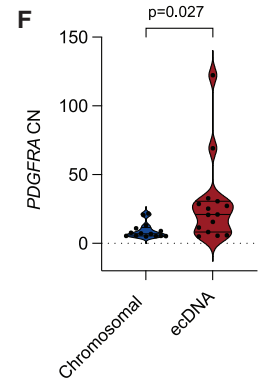
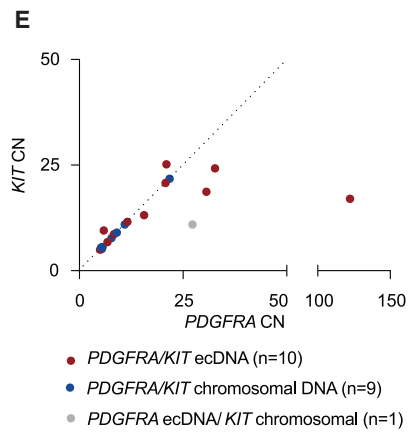
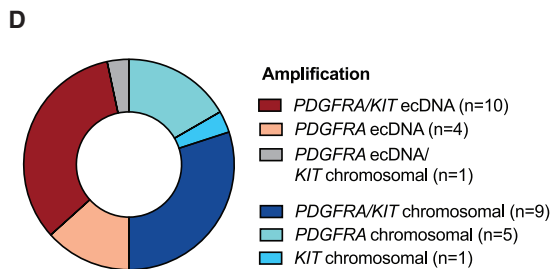
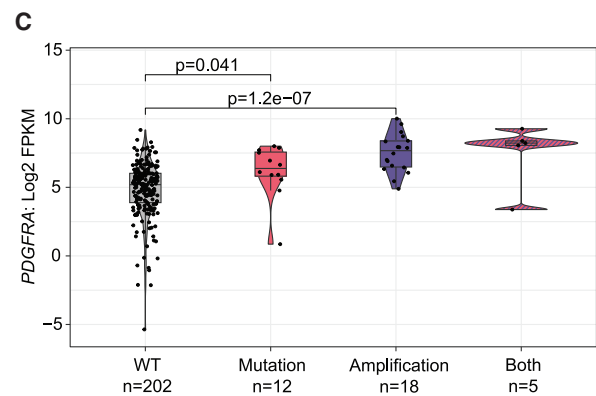
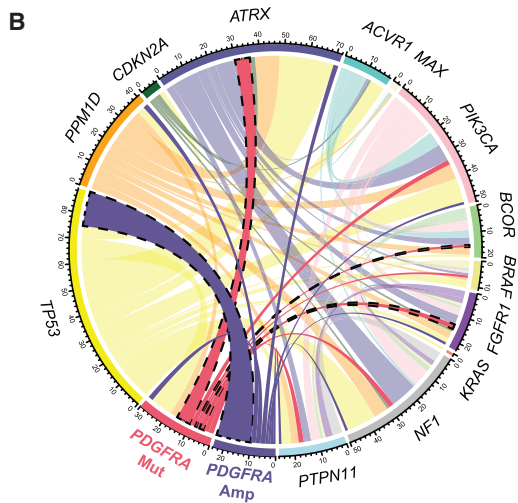
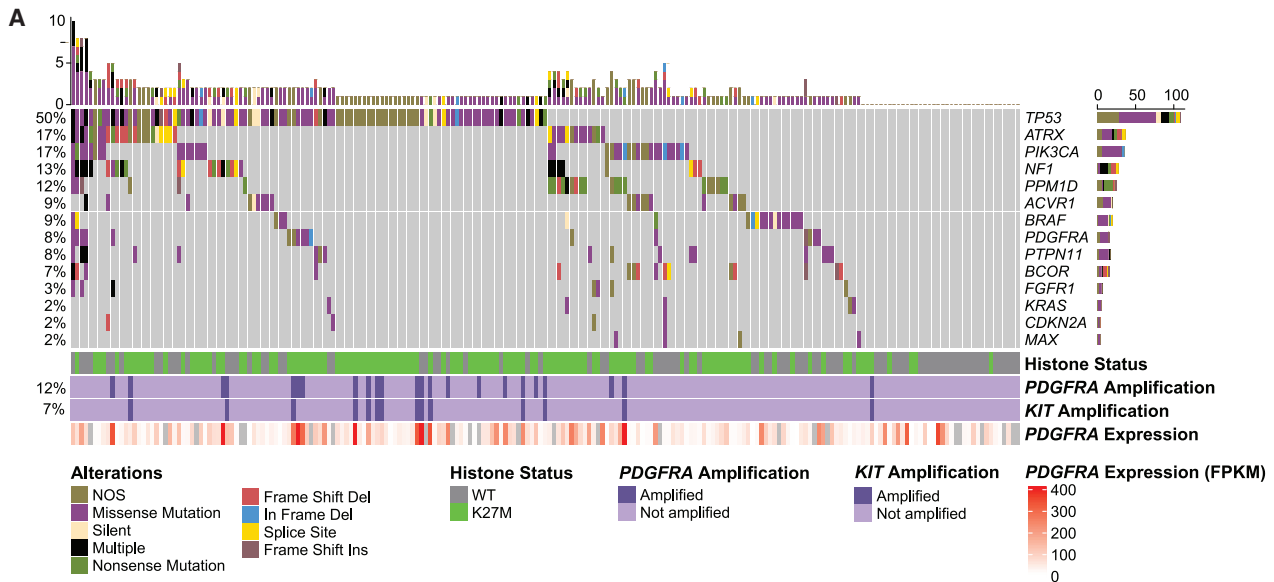
acts as a crucial oncogenic driver in the generation of DMG-like tumors in genetically engineered mouse models.<sup>9–11</sup> Third, single-cell transcriptomics of pediatric H3K27M DMG tumors revealed that elevated *PDGFRA* expression is a key defining feature of the cycling, stem-like population driving tumor growth, further highlighting its importance in the underlying biology of these tumors.<sup>9,12–15</sup> Together, these data suggest *PDGFRA* as a promising therapeutic target in the treatment of HGG. However, prior attempts to target *PDGFRA* in HGG with tyrosine kinase inhibitors (TKIs) such as dasatinib have been clinically unsuccessful, likely due to poor tolerability and lack of central nervous system (CNS) drug penetration.<sup>16–20</sup> Avapritinib, a next-generation TKI, is a highly selective small molecule inhibitor of *PDGFRA/KIT* and is currently approved by Food and Drug Administration (FDA) for adult patients with unresectable or metastatic gastrointestinal stromal tumors (GISTs) harboring *PDGFRA* exon 18 mutations, adult patients with indolent systemic mastocytosis (ISM), and adult patients with advanced systemic mastocytosis (AdvSM).<sup>21</sup>

Here, we set out to evaluate the pre-clinical efficacy, downstream effects, and pharmacokinetics as well as the early clinical impact of avapritinib in *PDGFRA*-altered HGG.

## RESULTS

### ***PDGFRA* mutations and amplifications, both leading to high *PDGFRA* expression, are common in pediatric high-grade glioma**

To determine the frequency of *PDGFRA* alterations in pHGG, we analyzed a comprehensive dataset combining unpublished genomic and transcriptomic data with publicly available sequencing datasets of pHGG (Tables S1 and S2,  $n = 261$ ). Of the 261 pHGG samples, genomic data with variant calling for commonly mutated genes was available for 217 samples (Figure 1A). We observed *PDGFRA* amplification and mutation in 7.3% ( $n = 19/261$ ) and 5.4% ( $n = 14/261$ ) of cases, respectively, with 1.9% of patients ( $n = 5/261$ ) harboring concurrent mutation and amplification (Table S3). In total, *PDGFRA*



(legend on next page)

genomic alterations were observed in 14.6% of patients (Table S3). *PDGFRA* point mutations occurred in all functional domains of the protein, with enrichment of mutations in the extracellular domain (Figure S1A). *PDGFRA* gene rearrangements, particularly *PDGFRA-KDR* fusions and *PDGFRA* exon 8–9 intragenic deletions, have been described as frequent events co-occurring with *PDGFRA* amplifications in adult GBM<sup>22</sup> and less frequently in pediatric HGG.<sup>8</sup> In our unpublished pHGG genomic cohort ( $n = 74$ ), no *PDGFRA-KDR* fusions or exon 8–9 deletions were detected. *PDGFRA* and *KIT* were frequently co-amplified, given their close proximity at the 4q12 locus (Figure 1A; Table S3). The frequency of *PDGFRA* amplification and/or mutations in H3 K27-altered and H3-wildtype/IDH-wildtype pHGG were 11.8% and 4.9%, respectively, for amplification and 5.6% and 9.9%, respectively, for mutations (Figure 1A). *PDGFRA* amplification was associated with *TP53* mutation, whereas *PDGFRA* mutations were observed frequently with *ATRX*, *BCOR*, or *FGFR1* mutations (Figure 1B). Transcriptomic data were available for 237 pHGG samples and revealed significantly elevated *PDGFRA* expression in tumors with *PDGFRA* mutation or amplification (Figure 1C).

Gene amplification may emerge as part of both the linear human chromosome as well as circular extrachromosomal amplicons (ecDNA). To assess the frequency and structural diversity of *PDGFRA* and *KIT* amplifications, a second genomic cohort with whole-genome sequencing (WGS) data of 388 pHGG/DMG patients (579 specimens) from two different pediatric cancer genomic data repositories was analyzed using previously published methods.<sup>23,24</sup> *PDGFRA* was frequently found on ecDNA amplicons with surrounding 4q DNA including *KIT* (Figure S1B). We identified 30 pediatric HGG patients with *PDGFRA* and/or *KIT* amplifications, including 20 cases in which the two genes were concomitantly amplified (Figure 1D; Table S4). In patients whose tumors had both *PDGFRA* and *KIT* amplifications, the majority showed equal *PDGFRA* and *KIT* copy numbers, with a small number of ecDNA-positive cases deviating from this pattern; one case had a *PDGFRA* copy number 7-fold higher than the *KIT* copy number (Figure 1E). ecDNA-positive amplifications showed significantly higher *PDGFRA* copy numbers compared to chromosomal counterparts (Figure 1F), demonstrating that all cases with >22 copies of *PDGFRA* or *KIT* were found on ecDNA.

Altogether, our genomic findings reinforce the important role of chromosomal and extrachromosomal oncogenic *PDGFRA* upregulation in pHGG, suggesting potential for *PDGFRA* pathway suppression as a therapeutic strategy in these patients.

### Avapritinib provides effective and selective PDGFRA targeting

We next sought to assess the efficacy and specificity of 2<sup>nd</sup> and 3<sup>rd</sup> generation *PDGFRA* inhibitors in HGG. Four compounds (dasatinib, crenolanib, axitinib, and avapritinib) were chosen based on FDA approval or active clinical trial investigation, known potency against *PDGFRA*, and/or prior clinical experience in HGG. We tested the activity of the aforementioned *PDGFRA* inhibitors against a panel of pediatric patient-derived or murine high-grade gliomasphere lines with *PDGFRA* alterations. Avapritinib exhibited the highest potency in the tested cell lines (Figure 2A). Using published data,<sup>25,26</sup> we generated kinome inhibition trees for these *PDGFRA* inhibitors to assess their specificity and observed fewest off-target kinases bound by avapritinib comparatively (Figure S1C). As prior studies of the *PDGFRA* inhibitor dasatinib have highlighted that off-target activity, particularly against SRC, ABL1, and KIT kinases, is associated with increased toxicity profiles in AML patients,<sup>27</sup> we performed additional *in vitro* kinase inhibition assays against these kinases. We observed reduced off-target kinase inhibition with avapritinib and crenolanib treatment compared to dasatinib (Figure S1D). Avapritinib inhibited wild-type KIT with an IC<sub>50</sub> of 245 nM, slightly higher than the previously reported value of 73 nM<sup>26</sup> (Figure S1D). Of note, *KIT* and *PDGFRA* are often co-amplified in pHGG, as previously published<sup>3</sup> and as demonstrated in our datasets (Figures 1A and 1D–1F), suggesting a possible benefit for dual kinase targeting.

We next performed cell-free kinase inhibition assays of three *PDGFRA* inhibitors (dasatinib, avapritinib, crenolanib) on wild-type and mutated *PDGFRA* (D842V and V561D) (Figure S1E). All inhibitors showed similar activity on wild-type and V561D *PDGFRA*. However, for D842V *PDGFRA*, avapritinib and crenolanib demonstrated 20-fold higher potency than dasatinib.

In summary, our pre-clinical data suggest avapritinib as a highly potent *PDGFRA* inhibitor, showing activity against mutant and amplified *PDGFRA* while exhibiting comparably reduced off-target kinase activity.

### Avapritinib exhibits potent inhibition and alters subcellular localization of PDGFRA across pediatric and adult PDGFRA-altered HGG models in vitro

Given the aforementioned data, we chose avapritinib for further testing in a panel of predominantly patient-derived *PDGFRA*-altered HGG and DMG cell models (Table S5). We included pediatric patient-derived HGG and DMG lines with *PDGFRA* gain/amplification (BT245, BT2159, R059) as well as patient-derived and murine models with D842V mutation in the activation loop domain (PPK) or V561 mutation in the juxtamembrane domain

#### Figure 1. *PDGFRA* is commonly altered and highly expressed in pediatric high-grade gliomas

(A) Oncoplot depicting mutations, *PDGFRA* amplification status, and *PDGFRA* expression in pediatric high-grade glioma patient samples ( $n = 217$ ). (B) Circos plot of *PDGFRA* amplification/mutation with co-occurring mutations in 13 genes in pHGG ( $n = 153$ ). Dashed lines highlight significantly co-occurring combinations. (C) *PDGFRA* expression by *PDGFRA* alteration status in pHGG ( $n = 237$ ). Boxplots indicate interquartile range with the median as a line in the middle and whiskers representing min/max values. Only significant  $p$  values are shown. Significance was assessed using  $t$  test. (D) Type of *PDGFRA* and/or *KIT* amplification (chromosomal vs. extrachromosomal) in pHGG samples ( $n = 30$ ). (E) *PDGFRA* and *KIT* copy numbers in pHGG with both *PDGFRA* and *KIT* amplification ( $n = 20$ ). (F) *PDGFRA* copy number in pHGG with chromosomal ( $n = 15$ ) vs. extrachromosomal ( $n = 15$ ) *PDGFRA* amplification. Thick line in violin plot represents median, and thin lines demarcate the interquartile range. Significance was assessed using  $t$  test. WT, wild type, ecDNA, extrachromosomal DNA, CN, copy number. See also Figure S1 and Tables S1, S2, S3, and S4.

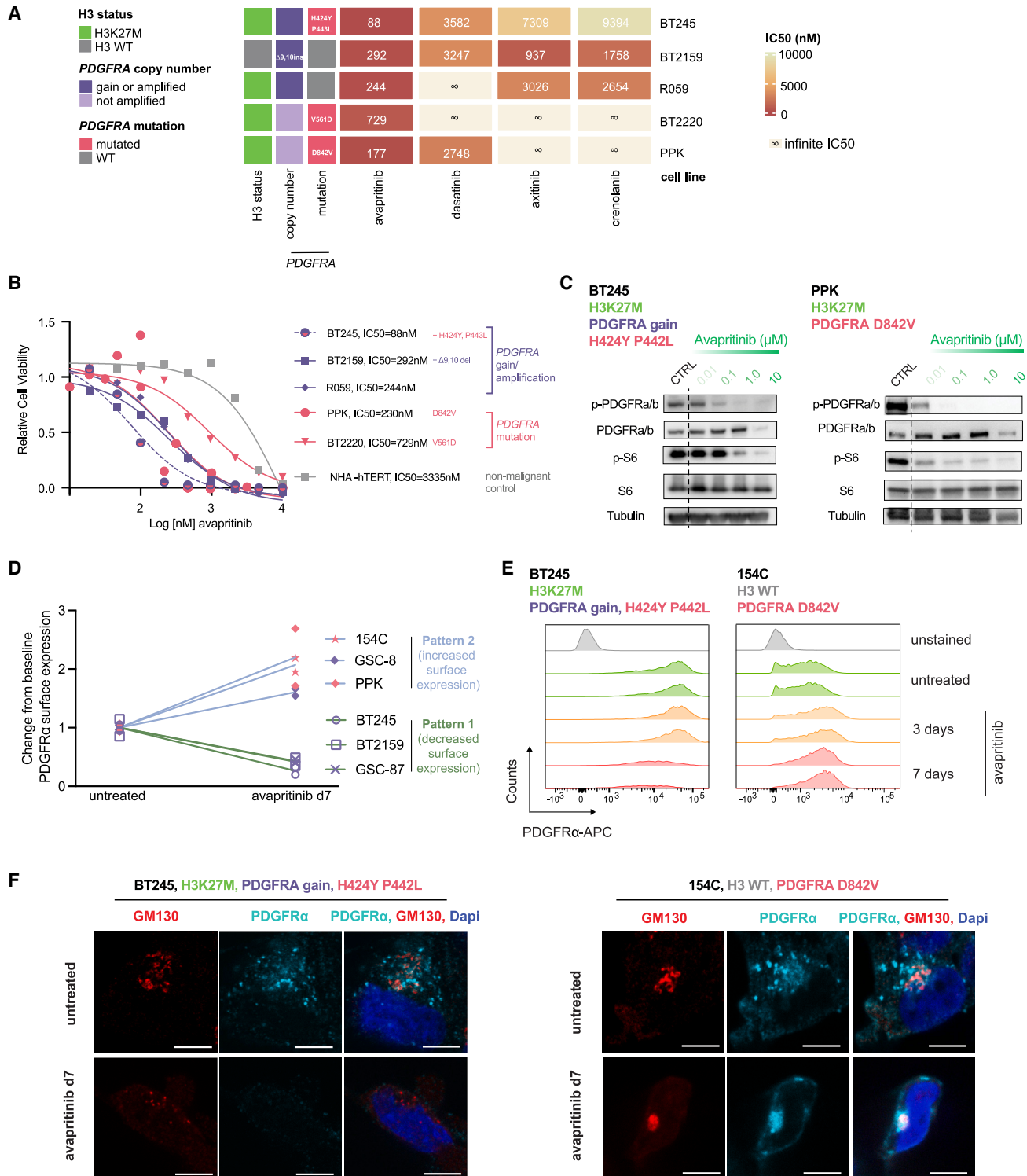


**Figure 2. Avapritinib decreases viability of PDGFRA-altered high-grade glioma *in vitro* and downregulates PDGFRA signaling**

(A) Average IC50 values after 7 days of PDGFRA inhibitor treatment. Two to three biological replicates (with  $n = 3-4$  technical replicates each) per cell line are shown in (B). Dose-response curves at 7 days following avapritinib treatment (on day 1 and 4). Mean values of two to three biological replicates (with  $n = 3-4$  technical replicates each) per cell line (C). Immunoblot analysis of total PDGFR $\alpha$ , phosphorylated PDGFR $\alpha$  (p-PDGFR $\alpha$ ), total S6, and phosphorylated S6 (p-S6) protein expression after 3 days of avapritinib treatment in BT245 and PPK cells. Immunoblot images have been cropped to show samples of interest and to align lanes. Representative images of one to two biological replicates are shown.

(legend continued on next page)

(BT2220), both of which have been described as constitutively activating.<sup>28</sup> Two of the models with *PDGFRA* gain harbored additional genomic *PDGFRA* alterations (H424Y and P443L mutations in BT245; exon 9–10 deletion in BT2159), which have not been functionally described yet.

We observed nanomolar range sensitivity across all tested pediatric *PDGFRA*-altered HGG and DMG cell lines. IC<sub>50</sub> values ranged from 80 to 700 nM at 7 days (Figures 2A and 2B). Non-malignant immortalized human astrocytes, although not directly representative of postnatal astrocytes, showed IC<sub>50</sub> values at 3 μM, suggesting selectivity for malignant cells (Figures 2A and 2B). Additionally, we tested avapritinib in patient-derived pediatric HGG cell lines with *PDGFRA* wild-type status as well as patient-derived adult HGG models with and without *PDGFRA* alteration (Figures S2A and S2B). While models with *PDGFRA* alteration (GSC-8, GSC-87, 154C) or overexpression (SU-DIPG XIIP\*) displayed sensitivity to avapritinib treatment, cell lines without *PDGFRA* activation were less sensitive (BT869 and GSC-4) or completely resistant (VBT125, VBT668, VBT92) (Figures S2A and S2B). Stimulation with varying amounts of PDGFA/B (no, low, normal, or ultra-high concentration) showed no ligand dependency of avapritinib sensitivity in the tested HGG and DMG cell lines (Figure S2C).

Immunoblot assessment demonstrated that avapritinib efficiently and persistently inhibits *PDGFRA* signaling across multiple *PDGFRA*-altered HGG models as evidenced by reduced expression of phosphorylated *PDGFRA* and phosphorylated S6 at 3 and 7 days (Figures 2C, S3A, and S3B). Phosphorylated S6 showed an increased expression at 1 μM avapritinib treatment after 7 days in a subset of cell lines, indicating rescue of downstream signaling through alternative pathways (Figure S3B). Expression of phosphorylated AKT was not affected at both time points (Figure S3C). After short-term avapritinib treatment (15 or 60 min), abolished *PDGFRA* phosphorylation was observed regardless of receptor stimulation with PDGFAA/BB (Figure S3D), whereas downstream S6 phosphorylation was restored after 60-min ligand stimulation in a subset of cell lines treated with short-term avapritinib (Figure S3D).

Mechanistically, avapritinib treatment resulted in increased apoptosis as evidenced by annexin V positivity (Figure S3E), whereas EdU incorporation did not show significant changes, suggesting that avapritinib does not significantly impact cell-cycle dynamics in *PDGFRA*-altered models (Figure S3F). In two cell lines with high-level *PDGFRA* amplification, short-term avapritinib treatment did not lead to significant changes in *PDGFRA* copy numbers, indicating that avapritinib might not selectively target cells with higher levels of amplification (Figure S3G).

Altogether, avapritinib treatment inhibits the growth of HGG and DMG models with *PDGFRA* amplification or activating mutation in a ligand-independent manner by blocking downstream *PDGFRA* signaling, resulting in increased apoptotic cell death.

Since certain *PDGFRA* alterations and pharmacological *PDGFRA* inhibition can influence intracellular trafficking and pro-

tein degradation of *PDGFRA*,<sup>28,29</sup> we next investigated the effect of avapritinib treatment on subcellular protein localization and stability of *PDGFRA*. Flow cytometry and immunostaining revealed two distinct patterns in response to avapritinib: In cell lines BT245, BT2159, and GSC-87 (all *PDGFRA* gain), we observed a similar pattern, termed “pattern 1.” In “pattern 1” cells, *PDGFRA* expression was diffuse at baseline, with no clear localization at the Golgi apparatus, and generally decreased after 7-day avapritinib treatment (Figures 2D, 2E, and S4A–S4C). Cell lines 154C (*PDGFRA* D842V mutation), GSC-8 (*PDGFRA* amplification), and PPK (*PDGFRA* D842V mutation) showed a distinct pattern, defined as “pattern 2.” In “pattern 2” cell lines, baseline *PDGFRA* co-localized with the Golgi apparatus marker GM130, as previously described for certain types of *PDGFRA* mutations,<sup>29,30</sup> and showed increased surface expression after 7-day avapritinib treatment in flow cytometry and immunofluorescence staining (Figures 2D–2F and S4A–S4C). Of note, the murine model PPK might display mechanistic subcellular effects not directly comparable to human pHGG cells, since the mutated *PDGFRA* is expressed under a strong promoter and was introduced by *in utero* electroporation, resulting in an unknown *PDGFRA* copy number and non-physiological gene regulation in these cells.

Following protein synthesis inhibition by cycloheximide in our models, BT245 cells (“pattern 1”) showed more stable protein levels after ligand stimulation but full ablation after avapritinib treatment (Figure S5A). In contrast, protein levels in 154C cells (“pattern 2”) decreased with ligand stimulation, with or without avapritinib treatment, when protein synthesis was inhibited (Figure S5A). Future studies are needed to determine whether the proposed model of distinct subcellular localization and protein stability patterns (Figure S5B) holds true for other cell lines and correlates with specific *PDGFRA* alterations.

Overall, our data indicate that avapritinib might elicit distinct mechanistic cellular effects in *PDGFRA*-altered cells, which awaits further investigation.

### Avapritinib treatment results in efficient brain penetrance and prolonged survival in *PDGFRA*-altered DMG models *in vivo*

We next asked whether avapritinib crosses the blood-brain barrier and impacts tumor growth in *PDGFRA*-altered glioma animal models. Pharmacokinetic analysis of avapritinib in non-tumor-bearing CD-1 mice showed a peak concentration of 10 μg/mL (20.08 μM) occurring at 2 h following one oral dose, with brain tissue concentrations reaching their maximum at 10 μM 2 h post-ingestion (Figure 3A). Independent pharmacokinetic analysis in wild-type C57BL6/J mice following a single dose showed peak plasma concentrations of approximately 10 μM at 6 h with a reduction in detectable levels to 10% of maximum after 24 h (Figure S6A). Following 8 days of daily avapritinib dosing to achieve steady state levels, brain tissues exhibited avapritinib concentrations of 1 μM, exceeding IC<sub>50</sub> values observed *in vitro* by 2- to 12-fold (Figure S6B).

(D) Change in *PDGFRA* surface expression compared to baseline measured by flow cytometry in PDGFAA/BB-starved cells treated with avapritinib for 7 days.

(E) Surface expression of *PDGFRα* measured by flow cytometry in two representative cell lines at the indicated time points.

(F) Representative images of subcellular expression of *PDGFRα* and co-localization with Golgi marker GM130 analyzed by immunofluorescence staining in two exemplary cell lines. Scale bar corresponds to 5 μM. See also Figures S2–S5 and Table S5.

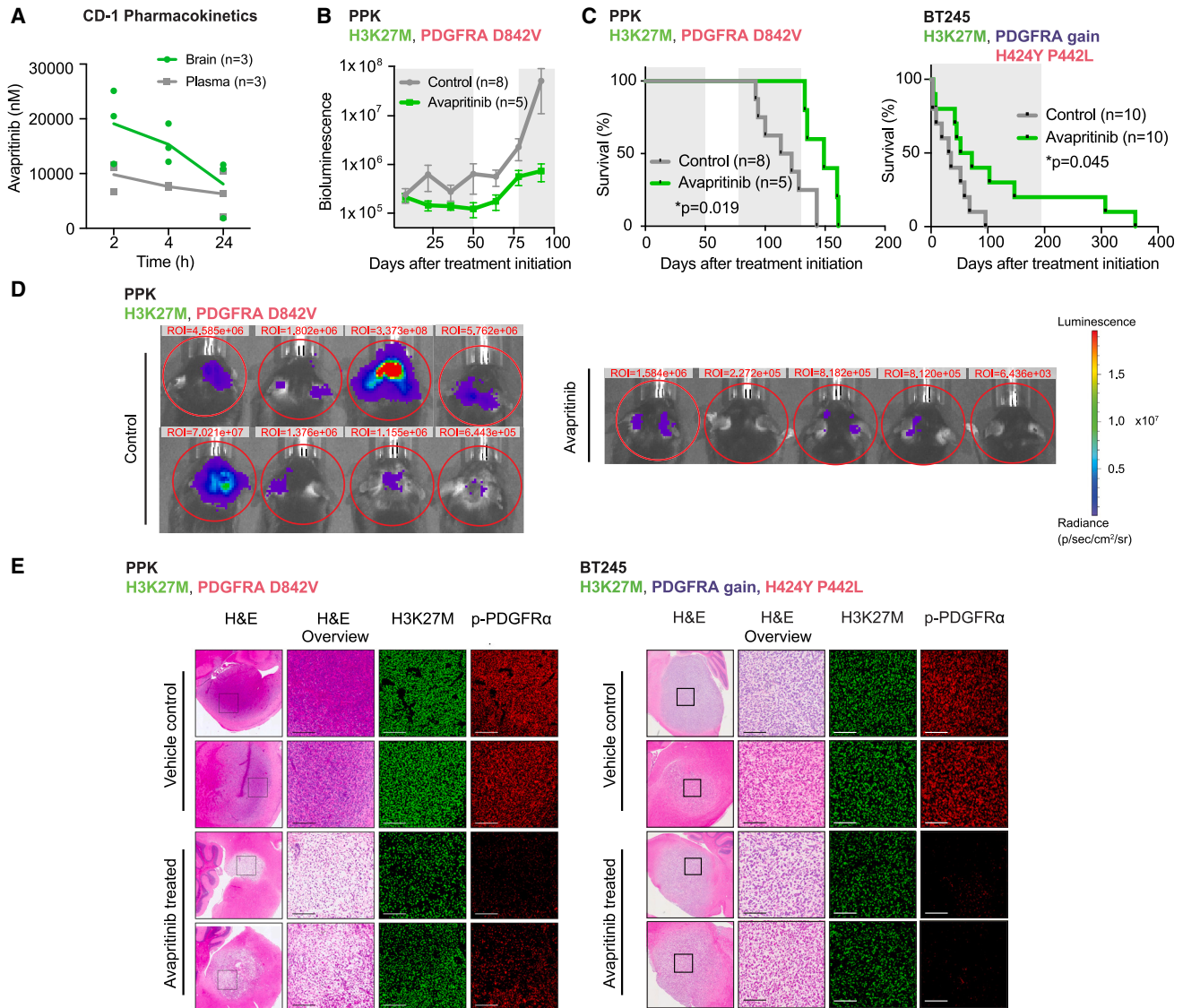


**Figure 3. Avapritinib shows efficient brain penetration and decreased tumor growth in PDGFRA-altered DMG models in vivo**

(A) Pharmacokinetic analysis of avapritinib concentrations in plasma and brain tissue in CD-1 mice after a single oral dose. Mean values are depicted by a line for each group.

(B) Bioluminescence measurement in vehicle or avapritinib-treated mice bearing PPK H3K27M DMGs. Median  $\pm$  SEM values are displayed. Gray background indicates period of treatment.

(C) Kaplan-Meier survival plots of PPK and BT245 H3K27M DMG xenografts following vehicle or avapritinib treatment. Gray background indicates period of treatment. Level of significance was calculated using the log rank (Mantel-Cox) test. Each mouse experiment was performed once per cell line with 5 to 10 animals per treatment group.

(D) Representative bioluminescence imaging at day 92 after start of treatment of mice bearing PPK H3K27M DMGs.

(E) Representative H&E and multiplexed immunofluorescence CODEX images of primary murine PPK (left) and patient-derived BT245 (right) DMG tumors, showing H3K27M expression and phosphorylated PDGFR $\alpha$  (p-PDGFR $\alpha$ ) expression following vehicle or avapritinib treatment. Scale bars indicate 100  $\mu$ m. See also [Figures S6](#) and [S7](#).

We then tested the effect of avapritinib treatment on tumor growth after establishment of tumors in two orthotopic HGG models with distinct *PDGFRA* alteration status: (1) “PPK”, a murine model with *TP53*, *PDGFRA* D842V, and H3K27M mutation,<sup>19</sup> and (2) BT245, a patient-derived H3K27M DMG xenograft model with *PDGFRA* gain and concomitant H424V and P443L mutation. Tumor growth was significantly reduced in avapritinib-treated mice bearing PPK tumors ([Figures 3B](#) and [3D](#)).

Avapritinib monotherapy conferred a significant survival benefit in both HGG models, extending median survival by 27% (PPK,  $n = 5-8$  per group,  $p = 0.019$ ) and 88% (BT245,  $n = 10$  per group,  $p = 0.045$ ) ([Figure 3C](#)). Notably, in BT245-bearing mice, avapritinib treatment resulted in long-term survival of two mice, extending beyond 200 days after avapritinib treatment, with evidence of

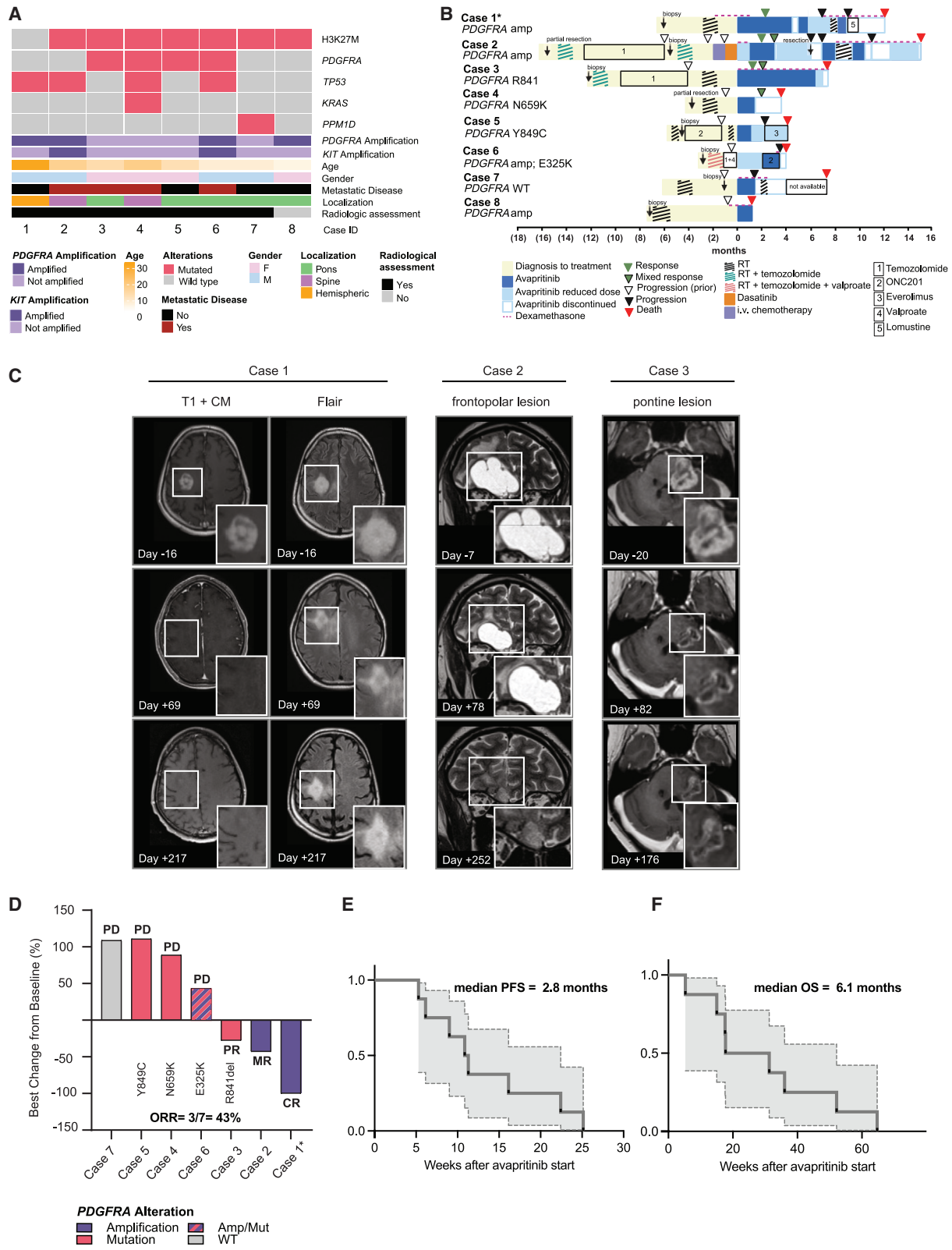


**Figure 4. Single agent avapritinib shows radiographic response in a subset of pediatric and young adult patients with PDGFRA-altered high-grade glioma**

(A) Clinical and molecular patient characteristics.

(legend continued on next page)

only minimal tumor growth 185 days following initiation of therapy (Figure 3C). We additionally investigated the effect of avapritinib treatment on survival in a third patient-derived H3K27M DMG model, SU-DIPG X11P\*. Although these cells genomically exhibit *PDGFRA* wild-type status, super-enhancer-driven over-expression of *PDGFRA* has been previously demonstrated.<sup>31</sup> In this highly aggressive model, avapritinib treatment resulted in a significantly extended median survival by 19% (Figure S6C,  $n = 4$  per group,  $p = 0.006$ ).

Avapritinib-treated PPK tumors exhibited downregulation of phosphorylated PDGFRA, phosphorylated S6, and Ki-67, confirming on-target inhibition of PDGFRA signaling with subsequent reduction in tumor cell proliferation after long-term treatment (Figures 3E, S6D, and S6E). In BT245 tumors, persistent downregulation of phosphorylated PDGFRA was observed (Figure 3E), whereas there was no significant difference in phosphorylated S6 and Ki-67, indicating active signaling via alternative pathways (Figures S6D and S6E). Phosphorylated AKT and ERK persisted in avapritinib-treated mice of both models, suggesting downstream activity independent of PDGFRA signaling in end-stage tumors as a potential compensatory mechanism (Figures S6E and S6F). We further assessed the effects of avapritinib on non-malignant cells *in vivo*. The abundance of non-malignant oligodendroglial cells ( $PDGFRA^+H3K27M^-$ ) did not differ between animals treated with the vehicle control and avapritinib (Figure S7A), potentially indicating the absence of significant toxicity on non-malignant cells of the oligodendroglial lineage in these mouse models.

In summary, we show that avapritinib efficiently crosses the blood-brain barrier to achieve supratherapeutic concentrations in target brain tissue. Furthermore, avapritinib treatment shows on-target PDGFRA signaling inhibition with reduced tumor growth and increased survival, providing pre-clinical rationale for the therapeutic use of avapritinib in HGG patients with *PDGFRA* activation.

### Avapritinib shows radiographic response in a subset of pediatric and young adult HGG patients with *PDGFRA* alterations

Following these encouraging pre-clinical results, our clinical centers initiated avapritinib treatment in patients through a compassionate use program, and we further combined our data with those from collaborators at multiple other institutions. Our real-world clinical dataset comprises detailed clinical follow-up of eight pediatric and young adult high-grade glioma patients

who were treated with avapritinib, along with first safety and outcome data. Patient demographics and tumor molecular alterations are summarized in Figure 4A; a detailed description of the individual treatment approaches for all patients is depicted in Table 1 and in Data S1.

Seven of eight patients had molecularly confirmed H3K27-altered DMG and showed progressive disease as assessed by RAPNO criteria before start of avapritinib treatment. In one young adult patient with hemispheric high-grade glioma, avapritinib was initiated as maintenance treatment shortly after radiotherapy (Case 1). Both genders were equally represented, and median patient age was 11 years (4–29 years). Tumors were located in the pons ( $n = 5$ ), spine ( $n = 2$ ), and hemispheres ( $n = 1$ ). Seven of eight patient tumors harbored *PDGFRA* alterations, including three tumors with *PDGFRA* amplification, three tumors with *PDGFRA* mutations (R841del, Y849C, N659K), and one tumor with a combined *PDGFRA* amplification and mutation (E325K). Two of the three patient tumors with *PDGFRA* amplification harbored concomitant *KIT* amplification. Metastatic disease was present in four patients at avapritinib treatment initiation. Four of eight cases in our series harbored somatic *TP53* mutations.

All patients received surgery (biopsy, partial or gross total resection) and local radiotherapy at primary diagnosis. Four of eight patients (Cases 2, 3, 5, and 6) were heavily pretreated before avapritinib treatment initiation with different approaches including temozolomide, dasatinib, intravenous chemotherapy, ONC201, and valproate, as depicted in the Swimmers plot in Figure 4B. Five patients (Cases 1, 2, 3, 7, and 8) received dexamethasone before and during the first avapritinib dosing, which was subsequently weaned off in four patients (Cases 1, 2, 7, and 8), and reduced in one patient (Case 3) throughout avapritinib treatment.

Avapritinib was administered orally once daily for a median duration of 4 months (1–10 months). To assess radiographic response, the first MRI after treatment initiation was performed at a median time of 69 days (36–105 days) after the start of avapritinib in all seven evaluable patients. Case 8 was unavailable for radiographic response assessment due to short survival after avapritinib initiation and was only included in the clinical response assessment. Avapritinib dosing ranged from 100 to 280 mg/m<sup>2</sup> (100–300 mg total doses). The most common adverse events included hair color change ( $n = 4$ ) and thrombocytopenia ( $n = 3$ ). Dose reduction occurred in four patients (Cases 1, 2, 3, and 5) and dose discontinuation occurred in three

(B) Swimmer's plot representing clinical course, and the individual treatment approach of all eight patients. Time 0 indicates initiation of avapritinib. Asterisk(\*) denotes histone wild-type case.

(C) Representative MRIs of responding patients depicting selected regressing target lesions prior to and throughout the course of avapritinib therapy. Date relative to avapritinib initiation. Evaluable target lesions are highlighted in the inserts with greater magnification. Of note, the FLAIR image for Case 1 at day +69 was sectioned at a different angle than the images at the other two time points; however, it is in the same location as the other two images.

(D) Waterfall plot depicting best response by RAPNO criteria of all target lesions combined for each patient following avapritinib therapy. Case 8 was unavailable for radiographic response assessment due to short survival after avapritinib initiation. For response assessment of non-pontine HGG (Cases 1, 2, and 4), RAPNO criteria for pHGG were used. For response assessment of pontine H3K27M DMG cases (Cases 3, 5, 6, and 7), specific RAPNO criteria for DIPG were used. CR, complete response, PR, partial response, MR, minor response, PD, progressive disease. Asterisk (\*) denotes histone wild-type case. ORR, objective response rate.

(E) Kaplan-Meier survival curve with 95% confidence interval (CI) depicting the progression-free survival (PFS) of all eight patients following initiation of avapritinib treatment.

(F) Kaplan-Meier survival curve with 95% confidence interval (CI) depicting the overall survival (OS) of all eight patients following initiation of avapritinib treatment. See also Figures S7 and S8 and Tables S6 and S7.

**Table 1. Clinical and molecular patient characteristics**

Case	Histologic diagnosis	Histone status	PDGFRA status	KIT status	Disease status at start of avapritinib	Radiation	Prior systemic therapies	Concurrent therapies	Other alterations
1	HGG	Wild type	Amplified	Wild type	Diagnosis	Yes	None	None	TP53, ATRX amplification
2	DMG	H3K27M	Amplified	Amplified	Recurrent/progressive	Yes	TMZ, dasatinib	None	TP53
3	DMG	H3K27M	R841 mutated	Wild type	Recurrent/progressive	Yes	TMZ, re-irradiation	None	None
4	DMG	H3K27M	N659K mutated	Wild type	Recurrent/progressive	Yes	None	None	TP53, KRAS
5	DMG	H3K27M	Y849C mutated	Wild type	Recurrent/progressive	yes	Re-irradiation, ONC201	Everolimus	None
6	DMG	H3K27M	Amplified, E325K mutated	Amplified	Recurrent/progressive	Yes	TMZ, valproate	ONC201	TP53
7	DMG	H3K27M	Wild type	Wild type	Recurrent/progressive	Yes	None	None	PPM1D
8	DMG	H3K27M	Amplified	Wild type	Recurrent/progressive	Yes	None	None	None

patients (Cases 1, 2, and 3) due to the following adverse events attributed to avapritinib: thrombocytopenia ( $n = 1$ , grade 3), elevated liver function enzymes ( $n = 1$ , grade 3;  $n = 2$ ; grade 4), and asymptomatic intratumoral hemorrhage ( $n = 1$ , Grade 1), as depicted in [Figure S7B](#). After treatment interruption, thrombocyte counts and liver function enzyme levels normalized during the treatment break, and avapritinib was re-initiated at a reduced dose (200–225 mg) in all patients. Grade 3 neutropenia was observed in one patient, for whom avapritinib treatment was continued at a reduced dose without treatment interruption (200 mg).

With respect to previously described adverse effects of avapritinib, no spontaneous intracranial hemorrhages were observed in our patient population. Two small intratumoral hemorrhages with no clinical significance occurred in Case 2 during treatment at the initial dose of 300 mg, which resulted in avapritinib therapy interruption for 7 days. There were no changes to the hemorrhagic lesions or occurrence of new lesion following re-initiation of treatment with avapritinib at 200 mg, which the patient received for 11 more months.

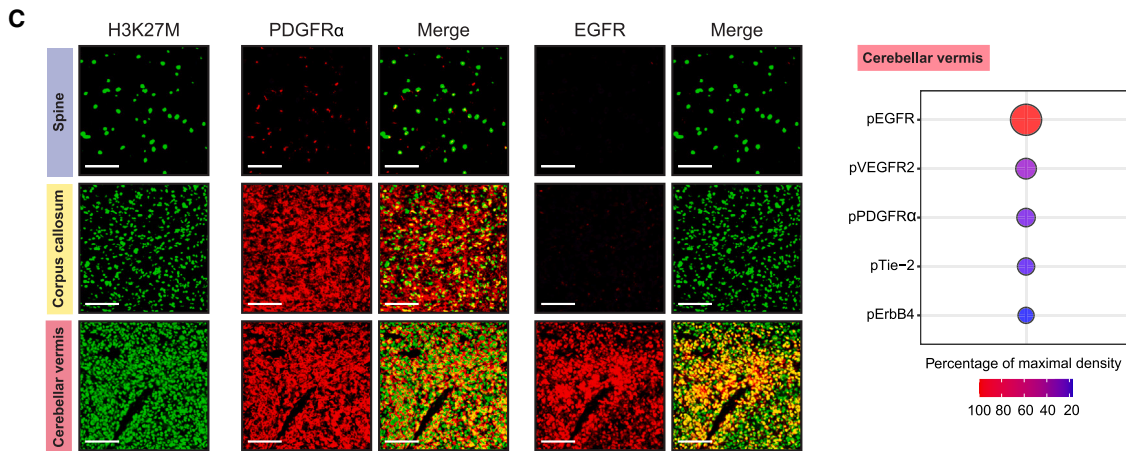
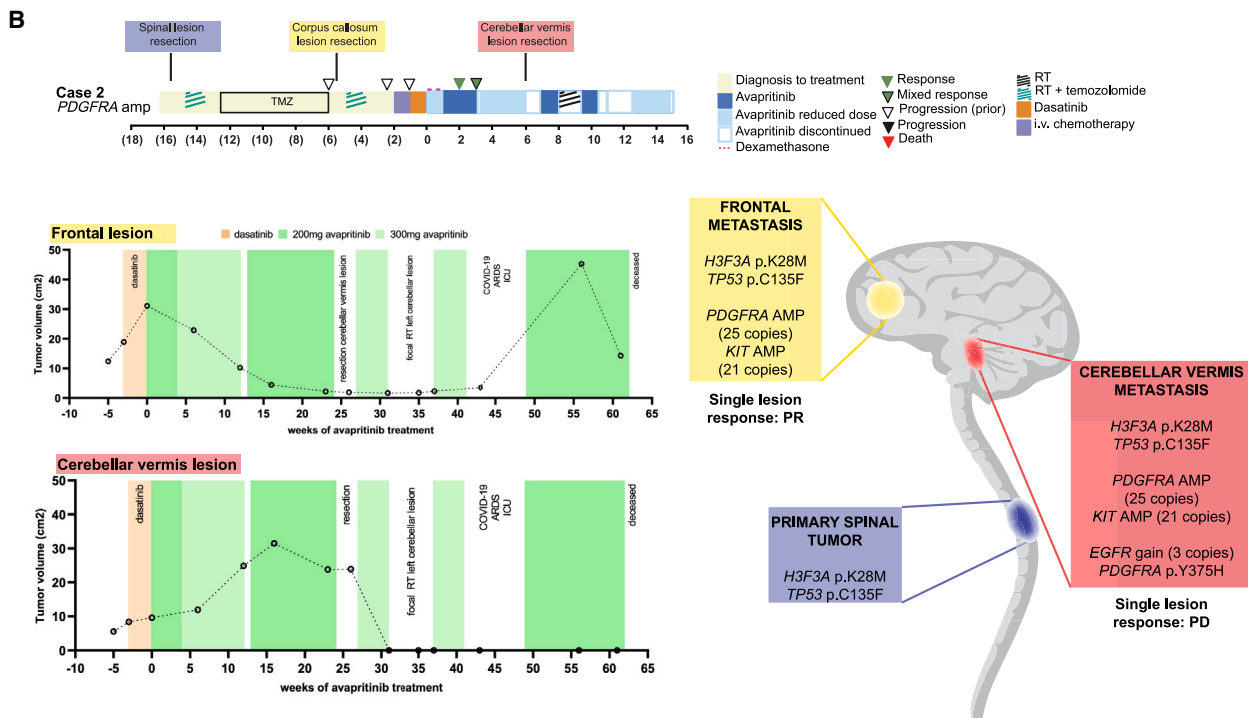
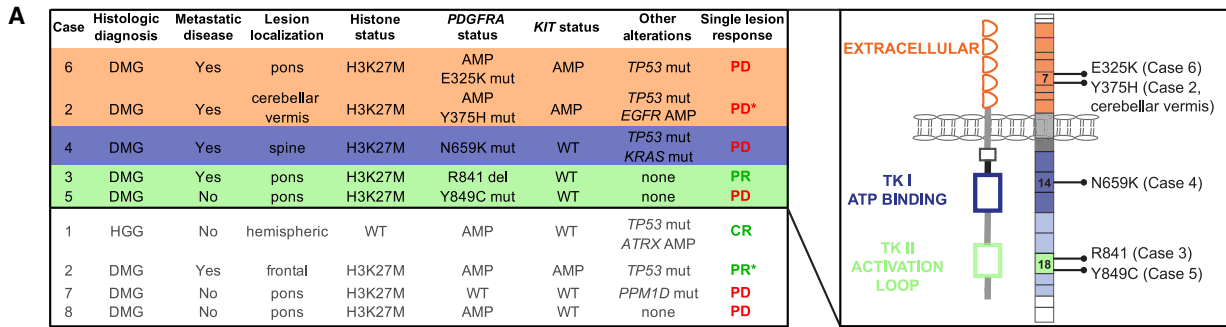
Neurocognitive testing in two heavily pretreated and irradiated brain tumor patients (Case 2 and Case 3) revealed overall lower intelligence scale (WISC V) in one case with previous irradiation of the frontal lobe (Case 2) but average memory performance in both cases ([Table S6](#)). Longitudinal testing in one case (Case 3) did not reveal changes upon avapritinib treatment.

Cerebrospinal fluid (CSF) was sampled in two patients (Cases 2 and 3) for pharmacokinetic testing. Case 2 demonstrated an increase in the CSF/plasma ratio during the course of treatment, with tumor tissue reaching a concentration of 4  $\mu$ M avapritinib following 6 months of treatment ([Figure S7C](#)). CSF levels of avapritinib (15–46 nM) in both cases were substantially higher compared to dasatinib levels in Case 2 ( $\sim$ 2 nM) ([Figure S7D](#)).

Seven of eight cases were evaluable by centralized response assessment by RAPNO criteria for pediatric HGG<sup>32</sup> and DIPG<sup>33</sup> ([Figure S8A](#); [Table S7](#)), and representative MRIs are shown in [Figure 4C](#) (responders), [Figure S8B](#) (metastatic lesions responders), and [Figure S8C](#) (non-responders). Objective radiographic response was detected in three of seven evaluable patients (42%; [Figure 4D](#)), with clinical response in three of eight patients (37.5%). Best response from baseline included com-

plete response (CR) in Case 1, a young adult HGG patient with *PDGFRA* amplification who started avapritinib treatment shortly after radiotherapy as maintenance therapy. Case 1 showed disappearance of all contrast-enhancing lesions with residual focal T2/FLAIR hyperintensity. Since this T2/FLAIR hyperintensity did not exhibit any mass effect or diffusion restriction, both the local radiologist and the independent radiologist in the central review process agreed that it was consistent with residual gliosis after radiation in this area, compatible with a complete response. The T2/FLAIR-positive lesion did not show re-growth at the time of progression when a metastatic lesion developed, further confirming a sustained response of the primary lesion, as indicated by the patient's T1 imaging sequence. Clinically, after 3 months of avapritinib treatment, the patient's left hemiplegia had almost completely resolved, and the patient was weaned off corticosteroids. For Case 2, a patient with metastasized spinal H3K27M DMG with *PDGFRA/KIT* amplification in the metastatic lesions, T2/FLAIR images assessed by RAPNO criteria revealed overall minor response (43% reduction in the sum of all three target lesion areas combined at 8 months of avapritinib treatment). Following avapritinib initiation, dexamethasone was discontinued without neurological or clinical deterioration of the patient. The third responder, a patient with H3K27M DIPG harboring a *PDGFRA* R841 deletion (Case 3), showed partial response (27% reduction in lesion area in T2/FLAIR images per RAPNO response criteria for DIPG<sup>33</sup>) and clinical and neurological stabilization. Across all eight patients, median progression-free survival (PFS) after the start of avapritinib was 2.8 months (1.3–7.6 months; [Figure 4E](#)) and median overall survival (OS) was 6.1 months (1.3–15.1 months; [Figure 4F](#)). For patients with radiographic response (Cases 1, 2, and 3), median PFS was 5.2 months (2.7–7.6 months; [Figure S8D](#)), and median OS was 12 months (7.3–15.1 months; [Figure S8E](#)) after the start of avapritinib treatment. All three responding patients developed metastatic lesions that did not respond to avapritinib treatment and ultimately succumbed to their disease while the primary responding lesions showed no signs of progression in the last available MRI.

Overall, these early results demonstrate general safety and CNS penetrance in a small cohort of pediatric and young adult HGG patients and indicate initial clinical response in a subset



(legend on next page)

of HGG patients with *PDGFRA* amplification or exon 18 mutations.

### Distinct genomic *PDGFRA* alterations potentially correlate with clinical response to avapritinib

We next sought to delineate how specific *PDGFRA* alterations as well as additional genomic alterations might correlate with response to avapritinib treatment in this clinical cohort.

Five of eight analyzed tumors harbored *PDGFRA* point mutations (Figure 5A). The sole responding *PDGFRA*-mutated tumor harbored an exon 18 activation loop R841 deletion. Non-responding tumors harbored mutations in the extracellular domain (E325K), the activation loop (Y849C), and the ATP binding domain (N659K), of which only the latter has previously been shown to be less sensitive to inhibition by avapritinib.<sup>34</sup> Mutations in the extracellular domain of *PDGFRA* have also been reported in GIST.<sup>28,35</sup> The Y849C activation loop mutation, previously undescribed, is predicted to interfere with *PDGFRA* receptor interface interactions ([dsysmap.irbbarcelona.org](https://dsysmap.irbbarcelona.org)). Two of three tumors harboring *PDGFRA* amplification without concomitant mutation (hemispheric lesion in Case 1 and frontal lesion in Case 2) showed complete or near-complete response.

To investigate potential alterations that potentially confer resistance to avapritinib, we performed multi-modal assessment of available tissue obtained from multiple lesions with different response to avapritinib treatment throughout the clinical course of Case 2. This patient harbored a spinal H3K27M DMG with subsequent intracranial metastasis and demonstrated an overall minor response (MR) by RAPNO criteria<sup>32</sup> (Figure 4D) with heterogeneous responses of the individual frontal and cerebellar vermis lesions (Figure S8A). The patient's frontal lesion, which harbored a *de novo PDGFRA/KIT* amplification, showed near-complete response to avapritinib treatment, with regrowth upon drug discontinuation and response following re-initiation (Figures 4B, 4C, and 5B [frontal lesion]). The metastatic cerebellar vermis lesion progressed throughout avapritinib treatment (Figures 4B, 5B [cerebellar vermis lesion], and S8B) and harbored a *de novo EGFR* gain (three copies) (Figure 5B). Immunofluorescence analysis of the primary tumor and metastatic lesions revealed total *PDGFRA* upregulation in both metastatic lesions correlating with the emergence of the *de novo PDGFRA* amplification (Figure 5C). However, *EGFR* overexpression (Figure 5C) and increased *EGFR* phosphorylation (Figures 5C and S8F) were only observed in the progressive, avapritinib-resistant cerebellar vermis lesion, suggesting *EGFR* pathway upregulation as a potential mechanism of *PDGFRA* inhibitor resistance in this

patient. Additionally, an extracellular domain *PDGFRA* Y375H mutation was detected in the cerebellar vermis lesion. As this exon was not covered in targeted genomic analysis of previously biopsied lesions, we could not determine if this mutation had been present earlier (Figures 5A and 5B).

Altogether, these findings suggest that the response in patients with *PDGFRA* amplification may reflect mechanistic cellular effects observed *in vitro*, although further clinical studies are required. Furthermore, the sustained response of the initially treated lesions suggests newly acquired resistance mechanisms such as new *EGFR* alterations in the metastatic lesions that allow escape from avapritinib treatment.

## DISCUSSION

Despite advances in uncovering the genomic landscape of high-grade gliomas, pediatric and young adult patients diagnosed with HGG or DMG continue to face a devastating prognosis. Clinical response in these patients has been dismal, with only few recent interventions including ONC201<sup>36–38</sup> and anti-GD2 CAR T cell therapy<sup>39</sup> showing early promise. Recent collective sequencing efforts have identified several key molecular drivers of these malignancies.<sup>5,40</sup> Among them, *PDGFRA* has emerged as a promising therapeutic target due to its frequent genomic alterations and its essential role in driving oncogenic signaling in pHGG.<sup>5,8,10,12,20,40</sup> To address the critical need for effective *PDGFRA*-targeted therapies, we evaluated next-generation TKIs and identified avapritinib as a potent, selective, and CNS-penetrable *PDGFRA* inhibitor in patient-derived HGG and DMG models with *PDGFRA* alterations. In a translational bench-to bedside approach, and in collaboration with our multi-institutional partners, we were able to evaluate the tolerability and preliminary outcomes of avapritinib treatment in eight pediatric and young adult patients with HGG or DMG.

Although avapritinib was developed to target the *PDGFRA* D842V mutation, our *in vitro* data show that HGG models with *PDGFRA* gain/amplification respond similarly well. Of note, since the patient-derived models used in this study represent tumors of various molecular subgroups, age groups, and with variable oncogenic co-mutations, we cannot rule out other biological factors that might influence avapritinib downstream effects and activity. Therefore, our conclusions regarding potential differences in the response to avapritinib across different *PDGFRA*-alterations are limited and will need further in-depth validation.

Within our patient cohort, avapritinib therapy was generally well tolerated, in line with published reports from adult GIST and AdvSM clinical trials.<sup>21,41,42</sup> Prior reports of intracranial

### Figure 5. Type of *PDGFRA* alteration and additional *EGFR* amplification potentially determine response to avapritinib

(A) Left: table depicting *PDGFRA* mutations occurring in our patient cohort and single-lesion-specific response to avapritinib treatment. Asterisk (\*) denotes response of single lesions in the same patient (Case 2 overall showed a minor response [MR]). Right: graphical overview of *PDGFRA* protein domains and the mutated amino acid residues in individual tumor lesions in our patient cohort.

(B) Case 2 lesion-specific molecular profile and response. Top: treatment overview for Case 2 with indicated time points of lesion collection. Bottom left: volumetric assessment of the different lesions of Case 2 throughout treatment. Bottom right: overview schematic showing the different molecular alterations and single-lesion-specific response of the tumor lesions of Case 2. The primary spinal tumor showed stable disease since the patient's primary treatment and was therefore not included in the patient's overall response assessment.

(C) Left: representative multiplexed immunofluorescence CODEX images of H3K27M, total *PDGFR $\alpha$* , and total *EGFR* in primary spinal tumor, corpus callosum metastasis, and cerebellar vermis lesion of Case 2 at resection. Scale bars indicate 100  $\mu$ m. Right: expression levels of top five phosphorylated receptor tyrosine kinases in the cerebellar vermis lesion of Case 2 measured by phosphoproteomics. Raw density values were first normalized to the negative control and then to the sample with highest density (pEGFR). See also Figure S8.

hemorrhage raised concern for at-risk patients with CNS tumors.<sup>21</sup> However, we observed only one case of intratumoral hemorrhage in our cohort, which was clinically insignificant and showed no change after rechallenging. Importantly, the baseline rate of intracranial hemorrhage in DMG patients is ~20%, suggesting that this bleeding event may be unrelated to avapritinib.<sup>43</sup>

We assessed the radiographic response to avapritinib treatment in seven patients and revealed minor, partial, or complete response in three of seven evaluable patients. Of note, the included patients represent a challenging, highly treatment-refractory cohort. The results reported here have led to the ongoing Rover study, a phase 1/2 multi-center single-arm study to evaluate safety, pharmacokinetics, and efficacy of avapritinib in pediatric solid tumors with *PDGFRA/KIT* activating mutations, amplification, or H3K27M DMGs (NCT04773782).

Within the limits of our small cohort, we have gained insights into potential genetic predictors of response to avapritinib. Our data suggest a previously unappreciated role for avapritinib in HGG patients with *PDGFRA* copy-number gains, which is associated with worse prognosis in children<sup>20</sup> and adults.<sup>44–46</sup> *KIT* is frequently co-amplified in patients with *PDGFRA* copy-number gains,<sup>47–49</sup> potentially enhancing response to a dual *KIT*/*PDGFRA* inhibitor such as avapritinib. One DMG case featuring wild-type *PDGFRA* showed no clear response to avapritinib therapy, suggesting that this patient population might benefit less from avapritinib treatment than DMG patients with concurrent *PDGFRA* amplifications or activation loop domain mutations.

Various acquired resistance mechanisms to TKI monotherapy have been described, including upregulation of alternative receptor tyrosine kinases, leading to reactivation of downstream signaling.<sup>50,51</sup> Here, the three patients with radiographic response eventually developed metastatic lesions resistant to avapritinib, whereas their primary responding lesions continued to show no signs of progression, suggesting new resistance mechanisms in the metastatic HGG lesions. In Case 2, molecular testing of the progressive cerebellar metastatic lesion revealed a *de novo EGFR* gain with increased EGFR expression and phosphorylation in the avapritinib-resistant tumor, indicating a potential escape mechanism due to the overlapping downstream signaling pathways between EGFR and *PDGFRA*. In addition to the activation of secondary “bypass” RTKs, RTK-independent activation of downstream pathways has also been identified as a resistance mechanism to TKIs therapy.<sup>51</sup> In our *in vitro* models, we observed sustained AKT phosphorylation and restored S6 phosphorylation in some models, suggesting activation of downstream signaling through other RTK. Long-term avapritinib-treated mice showed persistent phosphorylated AKT and ERK, indicating downstream activity independent of *PDGFRA* signaling in end-stage tumors. These findings highlight the need for combinatorial targeted therapy to combat treatment resistance and promote long-term survival. Based on our preliminary data, preclinical exploration of avapritinib in combination with EGFR inhibitors or compounds targeting the MAPK or PI3K pathways could reveal potential synergistic or additive combination strategies for further clinical evaluation.

Overall, our initial outcomes with avapritinib reveal an oral, targeted anti-cancer agent that provides response in a subset of treatment refractory patients. While generalizability is limited based on the small case number of this report, our results suggest a potential role for avapritinib in the treatment of HGG, particularly for patients with tumors with distinct *PDGFRA* alterations.

### Limitations of the study

Although our pre-clinical and clinical data are encouraging, several questions and potential limitations remain. First, these are results in a small cohort of patients and thus conclusions regarding biomarkers or genomic signatures predicting response need further evaluation in future clinical studies. Additionally, although we observed complete or near-complete radiological response in some cases/lesions, this report does not address the duration of avapritinib therapy required for durability of response. Although we observe no decrease in non-malignant oligodendroglial cells in our *in vivo* models and no significant acute neuro-cognitive toxicities in our patient cohort, given the high expression of *PDGFRA* in normal OPCs<sup>52,53</sup> and the importance of *PDGFRA* signaling in normal OPC development<sup>54,55</sup> and myelination,<sup>53,56</sup> the potential neurocognitive effects of long-term therapy in the pediatric population will need to be carefully assessed in upcoming clinical studies.

### RESOURCE AVAILABILITY

#### Lead contact

Further information and requests for resources and reagents should be directed to and will be fulfilled by the lead contact, Prof. Mariella Filbin ([mariella.filbin@childrens.harvard.edu](mailto:mariella.filbin@childrens.harvard.edu)).

#### Materials availability

PPK cells ([I] PBase, [II] PB-CAG-DNp53-Ires-Luciferase (dominant negative TP53 or TP53 hereafter), [III] PB-CAG-PdgfraD824V-Ires-eGFP (*PDGFRA* D842V), and [IV] PB-CAG-H3.3 K27M-Ires-eGFP (H3K27M)) are available upon request from Prof. Carl Koschmann.

#### Data and code availability

Published pHGG genomic datasets analyzed for *PDGFRA* alterations are included in previous work<sup>57,58</sup> and at the Children’s Brain Tumor Network ([www.cbtn.org](http://www.cbtn.org)). Unpublished data of 69 samples sequenced through the Michigan Oncology Sequencing Center (MI-ONCOSEQ) are available in Table S2.

For the second genomic analysis, focusing specifically on chromosomal and extrachromosomal *PDGFRA* amplifications, WGS data from the CBTN and St. Jude datasets are available from the following sources upon approval from an institutional data access committee. CBTN patient cohort: Kids First Data Resource Center (<https://kidsfirstdrc.org>) via the CAVATICA data portal. Inclusion criteria were all patient tumors with WGS in the PBTA-PNOC and PBTA-CBTN datasets, excluding the X01 subset. St. Jude patient cohort: St. Jude Cloud (<https://www.stjude.cloud>). Inclusion criteria were all patient tumors with WGS from the Pediatric Cancer Genome Project (PCGP, SJC-DS-1001) and Real-Time Clinical Genomics (RTCG, SJC-DS-1007) datasets as of March 2020. For this analysis focusing specifically on chromosomal and extrachromosomal *PDGFRA* amplifications, Code for the AmpliconArchitect family of software tools is available at <https://github.com/AmpliconSuite/AmpliconSuite-pipeline>. Code to regenerate all analyses and figures herein is available at [https://github.com/auberginekenobi/pedpancan\\_ecdna](https://github.com/auberginekenobi/pedpancan_ecdna).

Any additional information required to reanalyze the data reported in this paper is available from the lead contact upon request.

## ACKNOWLEDGMENTS

We thank Leonie Mikael for the helpful review of the manuscript. We acknowledge the support of Antony Hsieh, Mikael L. Rinne, Nina Perez, Saša Dimitrijević, and Sean Kim from Blueprint Medicines Corporation for their involvement in human avapritinib pharmacokinetic data generation and their review of this manuscript. We further thank Georg Schröckenfuchs, Dominik Kirchofer, Carola Jaunecker, and Johannes Hainfellner for their support of this study. Several figures were created with [BioRender.com](https://BioRender.com).

This work was supported by Sajni Chakrabarti Fund for Pediatric Brain Cancer Research (M.G.F.), Caroline Mortimer Fund (M.G.F.), DMG Precision Medicine Collaborative (M.G.F.), Claudia Adams Barr Program (M.G.F.), Cuming Family Fund for Pediatric Brain Tumor Research (M.G.F.), Anita, Sophia, and Athena Fund to Advance DIPG Research and Care (M.G.F.), Liv Like A Unicorn (M.G.F.), We love you Connie Fund (M.G.F.), MaleiaStrong Foundation (M.G.F.), The Morris Family (M.G.F.) and the DIPG All-In Initiative (M.G.F.). M.G.F. holds a NIH Director's New Innovator Award (DP2NS127705), a Career Award for Medical Scientist from the Burroughs Wellcome Fund, the Distinguished Scientist Award from the Sontag Foundation, the Helen Gurley Brown Foundation Helen Gurley Brown Presidential Initiative at Dana-Farber Cancer Institute, and the A-Award from the Alex's Lemonade Stand Foundation. M.G.F. was also supported by National Cancer Institute SPORE grant P50CA165962 and by National Cancer Institute U54 grant CA274516. C.K. was supported by National Institutes of Health Grant R01-NS119231 and R01-NS124607, DOD Grant CA201129P1, University of Michigan Chad Carr Pediatric Brain Tumor Center, Evans Family, ChadTough Defeat DIPG Foundation, Catching Up with Jack, Pediatric Brain Tumor Foundation, Michael Miller Memorial Foundation, Morgan Behen Golf Classic, and Yuvaan Tiwari Foundation. J.G. was supported by Forschungsgesellschaft fuer cerebrale Tumore and Verein unser\_kind. Other funding sources were Physician Researcher Pathway Scholarship of the Medical University of Vienna (L.M.), the Medical-scientific fund of the Mayor of the federal capital Vienna (project #19086, L.M.), the Austrian Science Fund (project T906-B28 to D.L.G. and P30105 to W.B.), Ministry of Health of the Czech Republic (Grant number NU20-03-00240; H.P., O.S., J.S.), and Walter Benjamin Program of the German Research Foundation (S.N.). C.J. was supported by Cancer Research UK, CRIS Cancer Foundation and Brain Tumour Research.

## AUTHOR CONTRIBUTIONS

Conceptualization, L.M., M.T., K.S., S.N., C.K., J.G., and M.G.F.; methodology, L.M., M.T., K.S., S.N., A.B., A.G., C.K., J.G., and M.G.F.; investigation, L.M., M.T., K.S., S.N., J.L., S.E., L.W.W., J.M., C.A.O.d.B.-J., C.L.C., O.C., S.S., R.K., A.D., S.W., J.W., O.H., A.N., C.M.N., S.C., J.S.R., A.G., E.P., G.A.V.C., R.D.H., K.T., J.W., A.T., S.K., M.M., P.T., K.B., D.S., A.L., A.S.G., J.S., H.P., J.N., N.S., V.R., C.D., A.B., O.S., P.P., L.M.C., A.C., Q.D.N., F.D., N.F.G., P.B., R.B., M.S., N.M., D.C.B., C.K.S., A.C., R.M., and J.F.; writing—original draft, L.M., M.T., K.S., and S.N.; writing—review & editing, L.M., M.T., K.S., S.N., A.B., A.G., C.K., J.G., and M.G.F.; funding acquisition, M.G.F., J.G., C.K., L.M., S.N., C.J., D.L.G., H.P., O.S., and J.S.; resources, K.L., C.K., N.J., A.B., S.B., A.G.S., S.M., D.T.W.J., C.J., J.S., L.M., C.H., S.M., D.L.G., M.S., B.W., U.L., K.D., A.P., A.A.A., H.K., L.C., C.K., J.G., and M.G.F.; supervision, C.K., J.G., and M.G.F.

## DECLARATION OF INTERESTS

Mariella G. Filbin was a consultant for Redona Therapeutics (previously named Twentyeight-Seven, Inc.) and Blueprint Medicines Corporation.

## STAR★METHODS

Detailed methods are provided in the online version of this paper and include the following:

- **KEY RESOURCES TABLE**
- **EXPERIMENTAL MODEL AND STUDY PARTICIPANT DETAILS**
  - Demographics and clinical monitoring of patients treated with avapritinib

- Informed consent and ethics
- *In vivo* models
- Cell lines
- **METHOD DETAILS**
  - *In silico* analysis of pediatric HGG samples
  - PDGFRA inhibitor testing in patient derived mouse and human *in vitro* models
  - *In vitro* kinase inhibition assays
  - Kinome tree generation
  - Immunoblots
  - PDGFRA flow cytometry
  - Immunofluorescence
  - Cell cycle and apoptosis assays
  - Cell line Nanopore WGS and copy number analysis
  - Orthotopic H3K27M mouse model experiments
  - Bioluminescence imaging (BLI)
  - Multiplexed immunofluorescence and image analysis of *in vivo* orthotopic tumor specimens and patient tumor tissue samples
  - Phosphoproteomics
  - C57/BL6J mouse pharmacokinetic analysis
  - CD1 mouse pharmacokinetic analysis
  - Patient pharmacokinetics
  - Neuropsychological assessment
- **QUANTIFICATION AND STATISTICAL ANALYSIS**

## SUPPLEMENTAL INFORMATION

Supplemental information can be found online at <https://doi.org/10.1016/j.ccell.2025.02.018>.

Received: July 30, 2024

Revised: November 27, 2024

Accepted: February 12, 2025

Published: March 13, 2025

## REFERENCES

1. Kaatsch, P. (2010). Epidemiology of childhood cancer. *Cancer Treat Rev.* 36, 277–285. <https://doi.org/10.1016/j.ctrv.2010.02.003>.
2. Pollack, I.F., Agnihotri, S., and Broniscer, A. (2019). Childhood brain tumors: current management, biological insights, and future directions. *J. Neurosurg. Pediatr.* 23, 261–273. <https://doi.org/10.3171/2018.10.PEDS18377>.
3. Ostrom, Q.T., Price, M., Ryan, K., Edelson, J., Neff, C., Cioffi, G., Waite, K.A., Kruchko, C., and Barnholtz-Sloan, J.S. (2022). CBTRUS Statistical Report: Pediatric Brain Tumor Foundation Childhood and Adolescent Primary Brain and Other Central Nervous System Tumors Diagnosed in the United States in 2014–2018. *Neuro Oncol.* 24, iii1–iii38. <https://doi.org/10.1093/neuonc/noac161>.
4. Organisation mondiale de la santé and Centre international de recherche sur le cancer (2021). *Central Nervous System Tumours, 5th ed. (International agency for research on cancer)*.
5. Mackay, A., Burford, A., Carvalho, D., Izquierdo, E., Fazal-Salom, J., Taylor, K.R., Bjerke, L., Clarke, M., Vinci, M., Nandhabalan, M., et al. (2017). Integrated Molecular Meta-Analysis of 1,000 Pediatric High-Grade and Diffuse Intrinsic Pontine Glioma. *Cancer Cell* 32, 520–537.e5. <https://doi.org/10.1016/j.ccell.2017.08.017>.
6. Wu, G., Broniscer, A., McEachron, T.A., Lu, C., Paugh, B.S., Becksfort, J., Qu, C., Ding, L., Huether, R., Parker, M., et al. (2012). Somatic histone H3 alterations in pediatric diffuse intrinsic pontine gliomas and non-brainstem glioblastomas. *Nat. Genet.* 44, 251–253. <https://doi.org/10.1038/ng.1102>.
7. Zarghooni, M., Bartels, U., Lee, E., Buczkowicz, P., Morrison, A., Huang, A., Bouffet, E., and Hawkins, C. (2010). Whole-genome profiling of pediatric diffuse intrinsic pontine gliomas highlights platelet-derived growth factor receptor alpha and poly (ADP-ribose) polymerase as potential therapeutic targets. *J. Clin. Oncol.* 28, 1337–1344. <https://doi.org/10.1200/JCO.2009.25.5463>.

8. Paugh, B.S., Zhu, X., Qu, C., Endersby, R., Diaz, A.K., Zhang, J., Bax, D.A., Carvalho, D., Reis, R.M., Onar-Thomas, A., et al. (2013). Novel oncogenic PDGFRA mutations in pediatric high-grade gliomas. *Cancer Res.* *73*, 6219–6229. <https://doi.org/10.1158/0008-5472.CAN-13-1491>.
9. Pathania, M., De Jay, N., Maestro, N., Harutyunyan, A.S., Nitarska, J., Pahlavan, P., Henderson, S., Mikael, L.G., Richard-Londt, A., Zhang, Y., et al. (2017). H3.3K27M Cooperates with Trp53 Loss and PDGFRA Gain in Mouse Embryonic Neural Progenitor Cells to Induce Invasive High-Grade Gliomas. *Cancer Cell* *32*, 684–700.e9. <https://doi.org/10.1016/j.ccell.2017.09.014>.
10. Larson, J.D., Kasper, L.H., Paugh, B.S., Jin, H., Wu, G., Kwon, C.-H., Fan, Y., Shaw, T.I., Silveira, A.B., Qu, C., et al. (2019). Histone H3.3 K27M Accelerates Spontaneous Brainstem Glioma and Drives Restricted Changes in Bivalent Gene Expression. *Cancer Cell* *35*, 140–155.e7. <https://doi.org/10.1016/j.ccell.2018.11.015>.
11. Tomita, Y., Shimazu, Y., Somasundaram, A., Tanaka, Y., Takata, N., Ishi, Y., Gadd, S., Hashizume, R., Angione, A., Pinerio, G., et al. (2022). A novel mouse model of diffuse midline glioma initiated in neonatal oligodendrocyte progenitor cells highlights cell-of-origin dependent effects of H3K27M. *Glia* *70*, 1681–1698. <https://doi.org/10.1002/glia.24189>.
12. Filbin, M.G., Tirosh, I., Hovestadt, V., Shaw, M.L., Escalante, L.E., Mathewson, N.D., Neftel, C., Frank, N., Pelton, K., Hebert, C.M., et al. (2018). Developmental and oncogenic programs in H3K27M gliomas dissected by single-cell RNA-seq. *Science* *360*, 331–335. <https://doi.org/10.1126/science.aao4750>.
13. Funato, K., Major, T., Lewis, P.W., Allis, C.D., and Tabar, V. (2014). Use of human embryonic stem cells to model pediatric gliomas with H3.3K27M histone mutation. *Science* *346*, 1529–1533. <https://doi.org/10.1126/science.1253799>.
14. Barton, K.L., Misuraca, K., Cordero, F., Dobrikova, E., Min, H.D., Gromeier, M., Kirsch, D.G., and Becher, O.J. (2013). PD-0332991, a CDK4/6 inhibitor, significantly prolongs survival in a genetically engineered mouse model of brainstem glioma. *PLoS One* *8*, e77639. <https://doi.org/10.1371/journal.pone.0077639>.
15. Patel, S.K., Hartley, R.M., Wei, X., Furnish, R., Escobar-Riquelme, F., Bear, H., Choi, K., Fuller, C., and Phoenix, T.N. (2020). Generation of diffuse intrinsic pontine glioma mouse models by brainstem-targeted in utero electroporation. *Neuro Oncol.* *22*, 381–392. <https://doi.org/10.1093/neuro/onc/noz197>.
16. Pollack, I.F., Jakacki, R.I., Blaney, S.M., Hancock, M.L., Kieran, M.W., Phillips, P., Kun, L.E., Friedman, H., Packer, R., Banerjee, A., et al. (2007). Phase I trial of imatinib in children with newly diagnosed brainstem and recurrent malignant gliomas: a Pediatric Brain Tumor Consortium report. *Neuro Oncol.* *9*, 145–160. <https://doi.org/10.1215/15228517-2006-031>.
17. Broniscer, A., Baker, S.D., Wetmore, C., Pai Panandiker, A.S., Huang, J., Davidoff, A.M., Onar-Thomas, A., Panetta, J.C., Chin, T.K., Merchant, T.E., et al. (2013). Phase I trial, pharmacokinetics, and pharmacodynamics of vandetanib and dasatinib in children with newly diagnosed diffuse intrinsic pontine glioma. *Clin. Cancer Res.* *19*, 3050–3058. <https://doi.org/10.1158/1078-0432.CCR-13-0306>.
18. Broniscer, A., Jia, S., Mandrell, B., Hamideh, D., Huang, J., Onar-Thomas, A., Gajjar, A., Raimondi, S.C., Tatevossian, R.G., and Stewart, C.F. (2018). Phase 1 trial, pharmacokinetics, and pharmacodynamics of dasatinib combined with crizotinib in children with recurrent or progressive high-grade and diffuse intrinsic pontine glioma. *Pediatr. Blood Cancer* *65*, e27035. <https://doi.org/10.1002/psc.27035>.
19. Miklja, Z., Yadav, V.N., Cartaxo, R.T., Siada, R., Thomas, C.C., Cummings, J.R., Mullan, B., Stallard, S., Paul, A., Bruzek, A.K., et al. (2020). Everolimus improves the efficacy of dasatinib in PDGFR $\alpha$ -driven glioma. *J. Clin. Investig.* *130*, 5313–5325. <https://doi.org/10.1172/JCI133310>.
20. Koschmann, C., Zamler, D., MacKay, A., Robinson, D., Wu, Y.-M., Doherty, R., Marini, B., Tran, D., Garton, H., Muraszko, K., et al. (2016). Characterizing and targeting PDGFRA alterations in pediatric high-grade glioma. *Oncotarget* *7*, 65696–65706. <https://doi.org/10.18632/oncotarget.11602>.
21. Heinrich, M.C., Jones, R.L., von Mehren, M., Schöffski, P., Serrano, C., Kang, Y.-K., Cassier, P.A., Mir, O., Eskens, F., Tap, W.D., et al. (2020). Avapritinib in advanced PDGFRA D842V-mutant gastrointestinal stromal tumour (NAVIGATOR): a multicentre, open-label, phase 1 trial. *Lancet Oncol.* *21*, 935–946. [https://doi.org/10.1016/S1470-2045\(20\)30269-2](https://doi.org/10.1016/S1470-2045(20)30269-2).
22. Ozawa, T., Brennan, C.W., Wang, L., Squatrito, M., Sasayama, T., Nakada, M., Huse, J.T., Pedraza, A., Utsuki, S., Yasui, Y., et al. (2010). PDGFRA gene rearrangements are frequent genetic events in PDGFRA-amplified glioblastomas. *Genes Dev.* *24*, 2205–2218. <https://doi.org/10.1101/gad.1972310>.
23. Deshpande, V., Luebeck, J., Nguyen, N.-P.D., Bakhtiari, M., Turner, K.M., Schwab, R., Carter, H., Mischel, P.S., and Bafna, V. (2019). Exploring the landscape of focal amplifications in cancer using AmpliconArchitect. *Nat. Commun.* *10*, 392. <https://doi.org/10.1038/s41467-018-08200-y>.
24. Chapman, O.S., Luebeck, J., Sridhar, S., Wong, I.T.-L., Dixit, D., Wang, S., Prasad, G., Rajkumar, U., Pagadala, M.S., Larson, J.D., et al. (2023). Circular extrachromosomal DNA promotes tumor heterogeneity in high-risk medulloblastoma. *Nat. Genet.* *55*, 2189–2199. <https://doi.org/10.1038/s41588-023-01551-3>.
25. Davis, M.I., Hunt, J.P., Herrgard, S., Ciceri, P., Wodicka, L.M., Pallares, G., Hocker, M., Treiber, D.K., and Zarrinkar, P.P. (2011). Comprehensive analysis of kinase inhibitor selectivity. *Nat. Biotechnol.* *29*, 1046–1051. <https://doi.org/10.1038/nbt.1990>.
26. Evans, E.K., Gardino, A.K., Kim, J.L., Hodous, B.L., Shutes, A., Davis, A., Zhu, X.J., Schmidt-Kittler, O., Wilson, D., Wilson, K., et al. (2017). A precision therapy against cancers driven by KIT/PDGFR mutations. *Sci. Transl. Med.* *9*, eaao1690. <https://doi.org/10.1126/scitranslmed.aao1690>.
27. Giles, F.J., O'Dwyer, M., and Swords, R. (2009). Class effects of tyrosine kinase inhibitors in the treatment of chronic myeloid leukemia. *Leukemia* *23*, 1698–1707. <https://doi.org/10.1038/leu.2009.111>.
28. Ip, C.K.M., Ng, P.K.S., Jeong, K.J., Shao, S.H., Ju, Z., Leonard, P.G., Hua, X., Vellano, C.P., Woessner, R., Sahni, N., et al. (2018). Neomorphic PDGFRA extracellular domain driver mutations are resistant to PDGFRA targeted therapies. *Nat. Commun.* *9*, 4583. <https://doi.org/10.1038/s41467-018-06949-w>.
29. Bahlawane, C., Eulenfeld, R., Wiesinger, M.Y., Wang, J., Muller, A., Girod, A., Nazarov, P.V., Felsch, K., Vallar, L., Sauter, T., et al. (2015). Constitutive activation of oncogenic PDGFR $\alpha$ -mutant proteins occurring in GIST patients induces receptor mislocalisation and alters PDGFR $\alpha$  signalling characteristics. *Cell Commun. Signal.* *13*, 21. <https://doi.org/10.1186/s12964-015-0096-8>.
30. Obata, Y., Horikawa, K., Takahashi, T., Akieda, Y., Tsujimoto, M., Fletcher, J.A., Esumi, H., Nishida, T., and Abe, R. (2017). Oncogenic signaling by Kit tyrosine kinase occurs selectively on the Golgi apparatus in gastrointestinal stromal tumors. *Oncogene* *36*, 3661–3672. <https://doi.org/10.1038/onc.2016.519>.
31. Nagaraja, S., Vitanza, N.A., Woo, P.J., Taylor, K.R., Liu, F., Zhang, L., Li, M., Meng, W., Ponnuswami, A., Sun, W., et al. (2017). Transcriptional Dependencies in Diffuse Intrinsic Pontine Glioma. *Cancer Cell* *31*, 635–652.e6. <https://doi.org/10.1016/j.ccell.2017.03.011>.
32. Erker, C., Tamrazi, B., Poussaint, T.Y., Mueller, S., Mata-Mbemba, D., Franceschi, E., Brandes, A.A., Rao, A., Haworth, K.B., Wen, P.Y., et al. (2020). Response assessment in paediatric high-grade glioma: recommendations from the Response Assessment in Pediatric Neuro-Oncology (RAPNO) working group. *Lancet Oncol.* *21*, e317–e329. [https://doi.org/10.1016/S1470-2045\(20\)30173-X](https://doi.org/10.1016/S1470-2045(20)30173-X).
33. Cooney, T.M., Cohen, K.J., Guimaraes, C.V., Dhall, G., Leach, J., Massimino, M., Erbetta, A., Chiapparini, L., Malbari, F., Kramer, K., et al. (2020). Response assessment in diffuse intrinsic pontine glioma: recommendations from the Response Assessment in Pediatric Neuro-Oncology (RAPNO) working group. *Lancet Oncol.* *21*, e330–e336. [https://doi.org/10.1016/S1470-2045\(20\)30166-2](https://doi.org/10.1016/S1470-2045(20)30166-2).

34. Grunewald, S., Klug, L.R., Mühlenberg, T., Lategahn, J., Falkenhorst, J., Town, A., Ehrh, C., Wardelmann, E., Hartmann, W., Schildhaus, H.-U., et al. (2021). Resistance to Avapritinib in PDGFRA-Driven GIST Is Caused by Secondary Mutations in the PDGFRA Kinase Domain. *Cancer Discov.* *11*, 108–125. <https://doi.org/10.1158/2159-8290.CD-20-0487>.
35. Amagai, Y., Matsuda, A., Jung, K., Oida, K., Jang, H., Ishizaka, S., Matsuda, H., and Tanaka, A. (2015). A point mutation in the extracellular domain of KIT promotes tumorigenesis of mast cells via ligand-independent auto-dimerization. *Sci. Rep.* *5*, 9775. <https://doi.org/10.1038/srep09775>.
36. Chi, A.S., Tarapore, R.S., Hall, M.D., Shonka, N., Gardner, S., Umemura, Y., Sumrall, A., Khatib, Z., Mueller, S., Kline, C., et al. (2019). Pediatric and adult H3 K27M-mutant diffuse midline glioma treated with the selective DRD2 antagonist ONC201. *J. Neuro Oncol.* *145*, 97–105. <https://doi.org/10.1007/s11060-019-03271-3>.
37. Hall, M.D., Oda, Y., Allen, J.E., Tarapore, R., Khatib, Z., Niazi, T.N., Daghistani, D., Schalop, L., Chi, A.S., Oster, W., and Mehta, M.P. (2019). First clinical experience with DRD2/3 antagonist ONC201 in H3 K27M-mutant pediatric diffuse intrinsic pontine glioma: a case report. *J. Neurosurg. Pediatr.* *23*, 719–725. <https://doi.org/10.3171/2019.2.PEDS18480>.
38. Venneti, S., Kawakibi, A.R., Ji, S., Waszak, S.M., Sweha, S.R., Mota, M., Pun, M., Deogharkar, A., Chung, C., Tarapore, R.S., et al. (2023). Clinical Efficacy of ONC201 in H3K27M-Mutant Diffuse Midline Gliomas Is Driven by Disruption of Integrated Metabolic and Epigenetic Pathways. *Cancer Discov.* *13*, 2370–2393. <https://doi.org/10.1158/2159-8290.CD-23-0131>.
39. Majzner, R.G., Ramakrishna, S., Yeom, K.W., Patel, S., Chinnasamy, H., Schultz, L.M., Richards, R.M., Jiang, L., Barsan, V., Mancusi, R., et al. (2022). GD2-CAR T cell therapy for H3K27M-mutated diffuse midline gliomas. *Nature* *603*, 934–941. <https://doi.org/10.1038/s41586-022-04489-4>.
40. Verhaak, R.G.W., Hoadley, K.A., Purdom, E., Wang, V., Qi, Y., Wilkerson, M.D., Miller, C.R., Ding, L., Golub, T., Mesirov, J.P., et al. (2010). Integrated genomic analysis identifies clinically relevant subtypes of glioblastoma characterized by abnormalities in PDGFRA, IDH1, EGFR, and NF1. *Cancer Cell* *17*, 98–110. <https://doi.org/10.1016/j.ccr.2009.12.020>.
41. Jones, R.L., Serrano, C., von Mehren, M., George, S., Heinrich, M.C., Kang, Y.-K., Schöffski, P., Cassier, P.A., Mir, O., Chawla, S.P., et al. (2021). Avapritinib in unresectable or metastatic PDGFRA D842V-mutant gastrointestinal stromal tumours: Long-term efficacy and safety data from the NAVIGATOR phase I trial. *Eur. J. Cancer* *145*, 132–142. <https://doi.org/10.1016/j.ejca.2020.12.008>.
42. Kang, Y.-K., George, S., Jones, R.L., Rutkowski, P., Shen, L., Mir, O., Patel, S., Zhou, Y., von Mehren, M., Hohenberger, P., et al. (2021). Avapritinib Versus Regorafenib in Locally Advanced Unresectable or Metastatic GI Stromal Tumor: A Randomized, Open-Label Phase III Study. *J. Clin. Oncol.* *39*, 3128–3139. <https://doi.org/10.1200/JCO.21.00217>.
43. Broniscer, A., Laningham, F.H., Kocak, M., Krasin, M.J., Fouladi, M., Merchant, T.E., Kun, L.E., Boyett, J.M., and Gajjar, A. (2006). Intratumoral hemorrhage among children with newly diagnosed, diffuse brainstem glioma. *Cancer* *106*, 1364–1371. <https://doi.org/10.1002/ncr.21749>.
44. Cancer Genome Atlas Research Network (2008). Comprehensive genomic characterization defines human glioblastoma genes and core pathways. *Nature* *455*, 1061–1068. <https://doi.org/10.1038/nature07385>.
45. Phillips, J.J., Aranda, D., Ellison, D.W., Judkins, A.R., Croul, S.E., Brat, D.J., Ligon, K.L., Horbinski, C., Venneti, S., Zadeh, G., et al. (2013). PDGFRA amplification is common in pediatric and adult high-grade astrocytomas and identifies a poor prognostic group in IDH1 mutant glioblastoma. *Brain Pathol.* *23*, 565–573. <https://doi.org/10.1111/bpa.12043>.
46. Higa, N., Akahane, T., Yokoyama, S., Yonezawa, H., Uchida, H., Takajo, T., Otsuji, R., Hamada, T., Matsuo, K., Kirishima, M., et al. (2022). Prognostic impact of PDGFRA gain/amplification and MGMT promoter methylation status in patients with IDH wild-type glioblastoma. *Neurooncol. Adv.* *4*, vdac097. <https://doi.org/10.1093/oaaj/ndvac097>.
47. Joensuu, H., Pupa, M., Sihto, H., Tynneninen, O., and Nupponen, N.N. (2005). Amplification of genes encoding KIT, PDGFRA and VEGFR2 receptor tyrosine kinases is frequent in glioblastoma multiforme. *J. Pathol.* *207*, 224–231. <https://doi.org/10.1002/path.1823>.
48. Nobusawa, S., Stawski, R., Kim, Y.-H., Nakazato, Y., and Ohgaki, H. (2011). Amplification of the PDGFRA, KIT and KDR genes in glioblastoma: a population-based study. *Neuropathology* *31*, 583–588. <https://doi.org/10.1111/j.1440-1789.2011.01204.x>.
49. Szerlip, N.J., Pedraza, A., Chakravarty, D., Azim, M., McGuire, J., Fang, Y., Ozawa, T., Holland, E.C., Huse, J.T., Jhanwar, S., et al. (2012). Intratumoral heterogeneity of receptor tyrosine kinases EGFR and PDGFRA amplification in glioblastoma defines subpopulations with distinct growth factor response. *Proc. Natl. Acad. Sci. USA* *109*, 3041–3046. <https://doi.org/10.1073/pnas.1114033109>.
50. Sierra, J.R., Cepero, V., and Giordano, S. (2010). Molecular mechanisms of acquired resistance to tyrosine kinase targeted therapy. *Mol. Cancer* *9*, 75. <https://doi.org/10.1186/1476-4598-9-75>.
51. Yang, Y., Li, S., Wang, Y., Zhao, Y., and Li, Q. (2022). Protein tyrosine kinase inhibitor resistance in malignant tumors: molecular mechanisms and future perspective. *Signal Transduct. Target. Ther.* *7*, 329. <https://doi.org/10.1038/s41392-022-01168-8>.
52. Marques, S., van Bruggen, D., Vanichkina, D.P., Floriddia, E.M., Munguba, H., Våremo, L., Giacomello, S., Falcão, A.M., Meijer, M., Björklund, Å.K., et al. (2018). Transcriptional Convergence of Oligodendrocyte Lineage Progenitors during Development. *Dev. Cell* *46*, 504–517.e7. <https://doi.org/10.1016/j.devcel.2018.07.005>.
53. Richardson, W.D., Pringle, N., Mosley, M.J., Westermarck, B., and Dubois-Dalq, M. (1988). A role for platelet-derived growth factor in normal gliogenesis in the central nervous system. *Cell* *53*, 309–319. [https://doi.org/10.1016/0092-8674\(88\)90392-3](https://doi.org/10.1016/0092-8674(88)90392-3).
54. van Heyningen, P., Calver, A.R., and Richardson, W.D. (2001). Control of progenitor cell number by mitogen supply and demand. *Curr. Biol.* *11*, 232–241. [https://doi.org/10.1016/s0960-9822\(01\)00075-6](https://doi.org/10.1016/s0960-9822(01)00075-6).
55. Zhu, Q., Zhao, X., Zheng, K., Li, H., Huang, H., Zhang, Z., Mastracci, T., Wegner, M., Chen, Y., Sussel, L., and Qiu, M. (2014). Genetic evidence that Nkx2.2 and Pdgfra are major determinants of the timing of oligodendrocyte differentiation in the developing CNS. *Development* *141*, 548–555. <https://doi.org/10.1242/dev.095323>.
56. Zhou, L., Shao, C.-Y., Xie, Y.-J., Wang, N., Xu, S.-M., Luo, B.-Y., Wu, Z.-Y., Ke, Y.H., Qiu, M., and Shen, Y. (2020). Gab1 mediates PDGF signaling and is essential to oligodendrocyte differentiation and CNS myelination. *Elife* *9*, e52056. <https://doi.org/10.7554/eLife.52056>.
57. Dubois, F.P.B., Shapira, O., Greenwald, N.F., Zack, T., Wala, J., Tsai, J.W., Crane, A., Baguette, A., Hadjadj, D., Harutyunyan, A.S., et al. (2022). Structural variants shape driver combinations and outcomes in pediatric high-grade glioma. *Nat. Cancer* *3*, 994–1011. <https://doi.org/10.1038/s43018-022-00403-z>.
58. van Tilburg, C.M., Pfaff, E., Pajtler, K.W., Langenberg, K.P.S., Fiesel, P., Jones, B.C., Balasubramanian, G.P., Stark, S., Johann, P.D., Blattner-Johnson, M., et al. (2021). The Pediatric Precision Oncology INFORM Registry: Clinical Outcome and Benefit for Patients with Very High-Evidence Targets. *Cancer Discov.* *11*, 2764–2779. <https://doi.org/10.1158/2159-8290.CD-21-0094>.
59. Patel, S.K., Hartley, R.M., Wei, X., Furnish, R., Escobar-Riquelme, F., Bear, H., Choi, K., Fuller, C., and Phoenix, T.N. (2020). Generation of diffuse intrinsic pontine glioma mouse models by brainstem targeted in utero electroporation. *Neuro Oncol.* *22*, 381–392. <https://doi.org/10.1093/neuonc/noz197>.
60. Panditharatna, E., Marques, J.G., Wang, T., Trissal, M.C., Liu, I., Jiang, L., Beck, A., Groves, A., Dharia, N.V., Li, D., et al. (2022). BAF Complex Maintains Glioma Stem Cells in Pediatric H3K27M Glioma. *Cancer*

- Discov. 12, 2880–2905. OF1–OF26. <https://doi.org/10.1158/2159-8290.CD-21-1491>.
61. Liao, B.B., Sievers, C., Donohue, L.K., Gillespie, S.M., Flavahan, W.A., Miller, T.E., Venteicher, A.S., Hebert, C.H., Carey, C.D., Rodig, S.J., et al. (2017). Adaptive Chromatin Remodeling Drives Glioblastoma Stem Cell Plasticity and Drug Tolerance. *Cell Stem Cell* 20, 233–246.e7. <https://doi.org/10.1016/j.stem.2016.11.003>.
62. Vaubel, R.A., Tian, S., Remonde, D., Schroeder, M.A., Mladek, A.C., Kitange, G.J., Caron, A., Kollmeyer, T.M., Grove, R., Peng, S., et al. (2020). Genomic and Phenotypic Characterization of a Broad Panel of Patient-Derived Xenografts Reflects the Diversity of Glioblastoma. *Clin. Cancer Res.* 26, 1094–1104. <https://doi.org/10.1158/1078-0432.CCR-19-0909>.
63. Garancher, A., Lin, C.Y., Morabito, M., Richer, W., Rocques, N., Larcher, M., Bihannic, L., Smith, K., Miquel, C., Leboucher, S., et al. (2018). NRL and CRX Define Photoreceptor Identity and Reveal Subgroup-Specific Dependencies in Medulloblastoma. *Cancer Cell* 33, 435–449.e6. <https://doi.org/10.1016/j.ccell.2018.02.006>.
64. Talevich, E., Shain, A.H., Botton, T., and Bastian, B.C. (2016). CNVkit: Genome-Wide Copy Number Detection and Visualization from Targeted DNA Sequencing. *PLoS Comput. Biol.* 12, e1004873. <https://doi.org/10.1371/journal.pcbi.1004873>.
65. Luebeck, J., Huang, E., Kim, F., Liefeld, T., Dameracharla, B., Ahuja, R., Schreyer, D., Prasad, G., Adamaszek, M., Kenkre, R., et al. (2024). AmpliconSuite: an end-to-end workflow for analyzing focal amplifications in cancer genomes. Preprint at: bioRxiv. <https://doi.org/10.1101/2024.05.06.592768>
66. Neradil, J., Kyr, M., Polaskova, K., Kren, L., Macigova, P., Skoda, J., Sterba, J., and Veselska, R. (2019). Phospho-Protein Arrays as Effective Tools for Screening Possible Targets for Kinase Inhibitors and Their Use in Precision Pediatric Oncology. *Front. Oncol.* 9, 930. <https://doi.org/10.3389/fonc.2019.00930>.
67. McDannold, N., Zhang, Y., Supko, J.G., Power, C., Sun, T., Peng, C., Vykhodtseva, N., Golby, A.J., and Reardon, D.A. (2019). Acoustic feedback enables safe and reliable carboplatin delivery across the blood-brain barrier with a clinical focused ultrasound system and improves survival in a rat glioma model. *Theranostics* 9, 6284–6299. <https://doi.org/10.7150/thno.35892>.
68. Petermann, F. (2016). WISC-V, Wechsler intelligence scale for children.
69. Lepach, A.C. (2008). Battery for Assessment in Children – Merk- und Lernfähigkeitstest.

## STAR★METHODS

### KEY RESOURCES TABLE

REAGENT or RESOURCE	SOURCE	IDENTIFIER
<b>Antibodies</b>		
anti-GM130	BD Biosciences	Cat# 610822; RRID:AB_398141
Goat anti-Mouse IgG (H+L) Cross-Adsorbed Secondary Antibody, Alexa Fluor™ 568	Thermo Fisher Scientific	Cat# A-11004; RRID:AB_2534072
Goat anti-Rabbit IgG (H+L) Cross-Adsorbed Secondary Antibody, Alexa Fluor™ 488	Thermo Fisher Scientific	Cat# A-11008; RRID:AB_143165
ProLong™ Diamond Antifade Mountant with DAPI	Thermo Fisher Scientific	Cat# P36962
anti-PDGFRα	Cell Signaling Technologies	Cat# 3174; RRID:AB_2162345
anti-phosphorylated-PDGFRα (Y754)	Cell Signaling Technologies	Cat# 2992; RRID:AB_390728
anti-S6	Cell Signaling Technologies	Cat# 2217; RRID:AB_331355
anti-phosphorylated-S6 (Ser 235/236)	Cell Signaling Technologies	Cat# 4858; RRID:AB_916156
anti-Alpha-Tubulin	Cell Signaling Technologies	Cat# 2125; RRID:AB_2619646
anti-AKT	Cell Signaling Technologies	Cat# 4691; RRID:AB_915783
anti-phosphorylated-AKT	Cell Signaling Technologies	Cat# 2992; RRID:AB_390728
HRP-linked anti-rabbit IgG	Cell Signaling Technologies	Cat# 7074S; RRID: AB_2099233
Recombinant Anti-Histone H3 (mutated K27M)	Abcam	Cat# ab190631; RRID:AB_2860570
Recombinant Anti-PDGFRα antibody	Abcam	Cat# ab234965; RRID:AB_2892065
Purified Mouse Anti-Ki-67 Clone B56	BD Biosciences	Cat# 550609; RRID:AB_393778
Human Anti-Phospho-PDGFRα (Y762)	R&D Systems	Cat# AF21141
anti-Phospho-S6 Ribosomal Protein (Ser240/244)	Cell Signaling Technologies	Cat# 5364S; RRID:AB_10694233
Phospho-Akt (Ser473)	Cell Signaling Technologies	Cat# 3787; RRID:AB_331170
EGFR	Thermo Fisher Scientific	Cat# MA513070; RRID:AB_10977527
Phospho-p44/42 MAPK (Erk1/2) (Thr202/Tyr204) (D13.14.4E)	Cell Signaling Technologies	Cat# 4370
Goat anti-Rabbit IgG (H+L) Cross-Adsorbed Secondary Antibody, HRP	Thermo Fisher Scientific	Cat# G21234
Goat anti-Mouse IgG (H+L) Cross-Adsorbed Secondary Antibody, HRP	Thermo Fisher Scientific	Cat# G21040
PDGFRA-APC (clone 16A1)	Thermo Fisher Scientific	Cat# NA15718; RRID:AB_2534498
Annexin V PerCP5.5	Biolegend	Cat# 640935
FxCycle Violet Stain	ThermoFisher	Cat# F10347
DAPI	Thermo Fisher Scientific	Cat# D1306; RRID:AB_2629482
<b>Biological samples</b>		
Patients and patient tumors	This paper	Table 1
<b>Chemicals, peptides, and recombinant proteins</b>		
B-27 supplement (50X), minus vitamin A	Thermo Fisher Scientific	Cat# 12587010
Recombinant H-EGF	Shenandoah Biotechnology Inc.	Cat# 100-26
Recombinant H-FGF-basic 154/FGF-2	Shenandoah Biotechnology Inc.	Cat# 100-18B
Recombinant H-PDGF-AA	Shenandoah Biotechnology Inc.	Cat# 100-16
Recombinant H-PDGF-BB	Shenandoah Biotechnology Inc.	Cat# 100-18
Heparin	Stem Cell Technologies	Cat# 07980
DMEM/F-12	Thermo Fisher Scientific	Cat# 11320033

(Continued on next page)

**Continued**

REAGENT or RESOURCE	SOURCE	IDENTIFIER
Neurobasal-A medium	Thermo Fisher Scientific	Cat# 10888022
Neurobasal Medium (1X)	Invitrogen	Cat# 21103-049
B27 Supplement (50X)	Invitrogen	Cat# 17504-044
N-2 Supplement (100X)	Invitrogen	Cat# 17502-048
Penicillin-Streptomycin	Invitrogen	Cat# 15140-122
IMDM	Thermo Fisher Scientific	Cat# 11514496
FBS	Thermo Fisher Scientific	Cat# A5256701
RPMI-1640	Thermo Fisher Scientific	Cat# 61870036
Sodium pyruvate solution	Invitrogen	Cat# 11360070
HEPES buffer	Invitrogen	Cat# 15630080
MEM non-essential amino acid solution	Thermo Fisher	Cat# 363401
GlutaMAX supplement	Invitrogen	Cat# 35050-061
Antibiotic-Antimycotic	Thermo Fisher	Cat# 15240062
Geltrex	Thermo Fisher	Cat# A1569601
Accutase	Thermo Fisher	Cat# A1569601
Sodium Pyruvate	Thermo Fisher	Cat# C809G58
Bovine Serum Albumin (BSA)	Biologend	Cat# 644710
Dimethyl sulfoxide (DMSO)	Sigma	Cat# 276855
D-PBS with CaCl and MgCl	Sigma	Cat# D-8662
PBS	Thermo Fisher	Cat# 10010023
RIPA Lysis Buffer	EMD Millipore	Cat# 20-188
PhosSTOP	Roche	Cat# 4906845001
cOmplete ULTRA Tablets, Mini	Roche	Cat# 5892791001
NuPAGE™ LDS Sample Buffer (4X)	Invitrogen	Cat# NP0007
DTT	Sigma	Cat# 10197777001
NuPAGE™ 4 to 12%, Bis-Tris, 1.0mm, 10well	LIFE TECHNOLOGIES CORP	Cat# NP0321BOX
NuPAGE™ MOPS SDS Running Buffer (20X)	LIFE TECHNOLOGIES CORP	Cat# NP0001
PageRuler™ Plus Prestained Protein Ladder, 10 to 250 kDa	Thermo Fisher	Cat# 26619
PVDF Western Blotting Membranes	Sigma	Cat# 3010040001
Western Blotting Filter Paper, 0.83 mm thick, 7 x 8.4 cm	LIFE TECHNOLOGIES CORP	Cat# 84783
NuPAGE Transfer Buffer (20x)	LIFE TECHNOLOGIES CORP	Cat# NP00061
Methanol	Sigma	Cat# 179957
Skim milk powder	Sigma	Cat# 1153630500
Restore Western blot Stripping buffer	Thermo Fisher	Cat# PI21059
10X TBS	BioRad	Cat# 1706435
Tween 20	BioRad	Cat# 1662404
SuperSignal West Pico PLUS ECL Reagent	LIFE TECHNOLOGIES CORP	Cat# 34580
SuperSignal™ West Dura Extended Duration Substrate	LIFE TECHNOLOGIES CORP	Cat# 34075
Annexin V binding buffer	Biologend	Cat# 422201
MACS® BSA Stock Solution	Miltenyi Biotec	Cat# 130-091-376
Paraformaldehyde 4%	LIFE TECHNOLOGIES CORP	Cat# J61899.AP
Normal Goat Serum Control	Thermo Fisher	Cat# 10000C
Triton X-100	Thermo Fisher	Cat# HFH10
Carboxymethylcellulose	Sigma	Cat# C5013-500G
Tween 80	Sigma	Cat# P1754-25ML
D-luciferin potassium salt	Promega	Cat# E1605
Acenonitrile	Sigma	Cat# 34851
Formic acide	Sigma	Cat# F0507

(Continued on next page)

**Continued**

REAGENT or RESOURCE	SOURCE	IDENTIFIER
Ammonium Formate	Sigma	Cat# 516961
non-enzymatic cell dissociation buffer	Thermo Fisher	Cat# 13151014
Cycloheximide	Selleckchem	Cat# S7418
TrypLE Express Enzyme (1X), no phenol	LIFE TECHNOLOGIES CORP	Cat# 12604013
Avapritinib	MedChemExpress	Cat# HY-101561
Dasatinib	MedChemExpress	Cat# HY-10181
Axitinib	MedChemExpress	Cat# HY-10065
Crenolanib	MedChemExpress	Cat# HY-13223
Cultrex Poly-D-Lysine	R&D Systems	Cat# 3439-200-01
Mouse laminin	Thermo Fisher	Cat# 23017015
Alexa Fluor® 647 azide	Invitrogen	Cat# A10277
ProLong™ Diamond Antifade Mountant with DAPI	Thermo Fisher	Cat# P36966

**Critical commercial assays**

Mycoplasma Detection Assay	Lonza	Cat# LT-07
CellTiter-Glo assay	Promega	Cat# G7571
Click-iT plus EdU Flow Cytometry Kit AF647	ThermoFisher	Cat# C10634
Pierce™ BCA Protein Assay Kit	ThermoFisher	Cat# 23227
XTT Cell Proliferation Assay kit	Cayman Chemical	Cat# 10010200
Opal Polaris 7 Color Manual IHC Detection Kit	Akoya BioSciences	Cat# OP-000003
Qiagen DNeasy Blood and Tissue DNA extraction kit	Qiagen	Cat# 69504
Human Phospho-RTK Array kit	R&D systems	Cat# ARY001B
Mouse Phospho-RTK Array kit	R&D systems	Cat# ARY014
ddPCR Copy Number Assay Kit	BioRad	Cat# dHsaCP1000047
MiniION & GridION Flow Cell (R10.4.1)	Nanopore	Cat# FLO-MIN114
Native Barcoding Kit 24 V14	Nanopore	Cat# SQK-NBD114.24
Z'LYTE Kinase Assay Kit (SelectScreen Profiling Services)	Thermo Fisher Scientific	Cat# PV3190

**Deposited data**

Original Western blot images	Mendeley	<a href="https://doi.org/10.17632/zwsndn95zn.1">https://doi.org/10.17632/zwsndn95zn.1</a>
Unpublished pHGG targeted sequencing data	This paper	Table S2
WGS data CBTN		<a href="https://cbtn.org/">https://cbtn.org/</a>
RNA sequencing data CBTN		<a href="https://cbtn.org/">https://cbtn.org/</a>
WGS sequencing data DFCI (Dubois et al., 2022)	dbGaP	phs002380.v1.p1
RNA sequencing data DFCI (Dubois et al., 2022)	dbGaP	phs002380.v1.p1
WES sequencing data INFORM (van Tilburg et al., 2021)	EGA	EGAS00001005112
RNA sequencing data INFORM (van Tilburg et al., 2021)	EGA	EGAS00001005112
WGS data St. Jude Cloud		<a href="https://www.stjude.cloud">https://www.stjude.cloud</a>

**Experimental models: Cell lines**

BT869	Boston Children's Hospital	N/A
BT2159	Boston Children's Hospital	N/A
BT2220	Boston Children's Hospital	N/A
BT245	Boston Children's Hospital	N/A
SU-DIPG XIIP*	Boston Children's Hospital	N/A
GSC-4	Massachusetts General Hospital	N/A
GSC-8	Massachusetts General Hospital	N/A
GSC-87	Massachusetts General Hospital	N/A
GBM-154C	Mayo Clinic	N/A

(Continued on next page)

**Continued**

REAGENT or RESOURCE	SOURCE	IDENTIFIER
QCTB-R059	Queensland Children's Medical Research Institute	N/A
NHA-hTERT	Massachusetts General Hospital	N/A
PPK	University of Michigan	N/A
VBT92	Medical University Vienna	N/A
VBT125	Medical University Vienna	N/A
VBT668	Medical University Vienna	N/A
<b>Experimental models: Organisms/strains</b>		
Mouse: NOD.Cg-Prkdc <sup>scid</sup> Il2rg <sup>tm1Wjl</sup> /SzJ	The Jackson Laboratory	RRID:IMSR_JAX:005557
Mouse: C57BL6/J	The Jackson Laboratory	RRID:IMSR_JAX:000664
Mouse: C.129S2-Cd1 <sup>tm1Gru</sup> /J	The Jackson Laboratory	RRID:IMSR_JAX:003814
<b>Recombinant DNA</b>		
pHIV-Luc-ZsGreen	Addgene	Cat# 39196; RRID:Addgene_39196
PBase	Tim Phoenix (University of Cincinnati)	N/A
PB-CAG-DNp53-Ires-Luciferase	Tim Phoenix (University of Cincinnati)	N/A
PB-CAG-PdgfraD824V-Ires-eGFP	Tim Phoenix (University of Cincinnati)	N/A
PB-CAG-H3.3 K27M-Ires-eGFP	Tim Phoenix (University of Cincinnati)	N/A
<b>Software and algorithms</b>		
GraphPad Prism 10	GraphPad Prism Software	RRID:SCR_002798
ImageJ	<a href="https://imagej.net/ij/">https://imagej.net/ij/</a>	v2.1.0; RRID: SCR_003070
KinMap	<a href="http://www.kinhub.org/kinmap/">http://www.kinhub.org/kinmap/</a>	
LINCS	<a href="https://lincs.hms.harvard.edu/">https://lincs.hms.harvard.edu/</a>	RRID:SCR_006454
Zen Microscopy Software	Zeiss	RRID:SCR_013672
FlowJo	BD Biosciences	RRID:SCR_008520
QuPath	<a href="https://qupath.github.io/">https://qupath.github.io/</a>	RRID:SCR_018257
inForm		RRID:SCR_019155
QuantaSoft software	Biorad	#1864011
R 4.0.1	<a href="https://www.r-project.org">https://www.r-project.org</a>	RRID:SCR_001905
guppy basecaller	<a href="https://github.com/timkahlke/LongRead_tutorials">https://github.com/timkahlke/LongRead_tutorials</a>	
minimap2	<a href="https://lh3.github.io/minimap2/minimap2.html">https://lh3.github.io/minimap2/minimap2.html</a>	
CoRAL	<a href="https://github.com/AmpliconSuite/CoRAL">https://github.com/AmpliconSuite/CoRAL</a>	
Biorender		RRID:SCR_018361

**EXPERIMENTAL MODEL AND STUDY PARTICIPANT DETAILS**

**Demographics and clinical monitoring of patients treated with avapritinib**

Eight patients (n=7 pediatric, n=1 young adult) were treated with avapritinib at a weight-based equivalent of the adult approved dose through compassionate use at the following institutions according to the expanded access compassionate-use program guidelines from Blueprint Medicines: General Hospital/Medical University of Vienna (n=2), University Children's Hospital Zurich (n=1), the University Medical Center Hamburg-Eppendorf (n=1), the Great North Children's Hospital (n=1), the University of Michigan Medical School (n=2), and Texas Children's Hospital (n=1). Patients included n=7 H3K27M DMG and n=1 WHO astrocytoma grade 3 cases. Seven of eight patient tumors harbored *PDGFRA* mutation and/or amplification; one H3K27M DMG case showed no detectable *PDGFRA* alteration. A detailed description of patients' demographics, sex and molecular alterations is depicted in [Table 1](#). Laboratory parameters were regularly assessed, and magnetic resonance imaging (MRI) was conducted per clinician discretion to monitor tumor response and further analyzed by central radiological assessment on the basis of the Response Assessment in Pediatric Neuro-Oncology (RAPNO) criteria for pGG<sup>32</sup> and DIPG.<sup>33</sup> All measurements are provided in [Table S7](#). MR Images of responders and non-responders are provided in [Figures 4C](#), [S8B](#), and [S8C](#).

**Informed consent and ethics**

This case series was approved by the local institutional review boards of the treating institutions. Informed consent was obtained for all patients and/or legal representatives.

### **In vivo models**

All animal studies were performed according to Dana-Farber Cancer Institute IACUC-approved protocols (08-023) or University of Michigan IACUC-approved protocols. For BT245- and SU-DIPG X11P<sup>-</sup>-PDX models, 6-week old female NSG mice (NOD.Cg-Prkdcscid Il2rgtm1Wjl/SzJ) were used. For the PPK-model, 6-week-old female C57BL6/J mice were used. Animals were assigned to the vehicle and treatment groups randomly.

### **Cell lines**

Mouse HGG primary “PPK” cells ([I] PBase, [II] PB-CAG-DNp53-Ires-Luciferase (dominant negative TP53 or TP53 hereafter), [III] PB-CAG-PdgfraD824V-Ires-eGFP (PDGFRA D842V), and [IV] PB-CAG-H3.3 K27M-Ires-eGFP (H3K27M)) were generated by harvesting intra-uterine electroporation (IUE) tumors at the time of euthanasia, using established methodology.<sup>19,59</sup> Tumors were located by green fluorescent protein (GFP) expression under an epi-fluorescent microscope (Olympus CKX41) at the time of resection. The tumor mass was gently homogenized and dissociated with non-enzymatic cell dissociation buffer (Gibco). Cell suspension was filtered through a 70 μm cell strainer, centrifuged at 300 x g for 4 min, and re-suspended into 7 ml of Neurobasal-A Medium (1x) Base media (Invitrogen, 500 mL). Each base stock of media was supplemented with 5 mL B27 without vitamin A, 5 mL Antibiotic-Antimycotic, 500 μL Heparin, 500 μL EGF (20ng/mL), 500 μL FGF (20ng/mL), 250 μL of PDGF-AA and PDGF-BB (10 ng/mL).

Patient derived glioma lines (BT245, BT2159, BT2220, 154C, R059) were grown as neurospheres in tumor stem media as described previously.<sup>60</sup> IUE-generated PDGFRA-driven HGG primary cell culture (PPK) were cultured in conditions as described above. Adult glioma lines GSC-8 and GSC-87 were grown in neurospheres in Neurobasal-A Medium (1x) Base media (Invitrogen, 500 mL) supplemented with 10 ml B-27, 2.5 ml N-2, 5 ml Antibiotic-Antimycotic, 7.5 ml GlutaMax, 500 μL EGF (20ng/mL), 500 μL FGF (20ng/mL) and 500 μL Heparin.<sup>61</sup> Immortalized normal human astrocytes (NHA-hTERT) were grown as adherent cultures in high glucose DMEM with 10% fetal bovine serum (FBS). The patient derived glioma VBT125 and VBT92 lines were cultured in RPMI-1640 medium with 10% FBS and the patient derived glioma line VBT668 was cultured in IMDM medium with 10% FBS. Cell lines were tested for mycoplasma every two months. QCTB-R059 cells were provided by Dr. Michelle Monje (Stanford) and initially generated by Dr Amy Moore’s lab (University of Queensland), Mayo 154C was derived from PDX models kindly provided by Dr. Jann Sarkaria.<sup>19,62</sup>

## **METHOD DETAILS**

### **In silico analysis of pediatric HGG samples**

For the first genomic analysis, focusing on identifying *PDGFRA* alterations in pHGG, we obtained previously published and unpublished genomic and transcriptomic data from pathologically confirmed pHGG samples (WHO grade 3 or 4 or H3K27M DMG, please refer to [Table S1](#) for a full list and references of datasets utilized). No H3 G34-mutant diffuse hemispheric gliomas were included in this analysis. Data of 69 previously unpublished patients sequenced through the Michigan Oncology Sequencing Center (MI-ONCOSEQ) are available in [Table S4](#). Variant calling for a curated set of HGG-related driver genes ([Figure 1A](#)) was available for 217 cases. Comprehensive expression, mutation, and *PDGFRA* variant analysis was available for a total of 237 cases. Variant annotation was performed using Functator (GATK v4.1.9.0). Additional analyses were performed in R (v4.1.0). Curated variants were visualized in an oncoplot using the package oncoprint (v0.1.1). All other visualizations were generated using ggplot2 (v3.3.5).

For the second analysis, focusing specifically on chromosomal and extrachromosomal *PDGFRA* amplifications in pHGG, Pediatric tumor WGS was identified from two pediatric cancer genomic data repositories, corresponding to 579 biosamples from 388 pHGG/DMG patients in the Children’s Brain Tumor Network (CBTN) and St Jude Cloud (SJC). Inclusion criteria were whole genome sequencing annotated with a tumor diagnosis; nontumor and unannotated samples were excluded. Data preprocessing comprised each institution’s standard WGS bioinformatics pipelines. To detect ecDNA, all samples in the WGS cohort were analyzed using AmpliconArchitect<sup>23</sup> v1.2 and AmpliconClassifier<sup>63</sup> v0.5.4. Briefly, the AmpliconArchitect algorithm was performed as follows. Copy number segmentation and estimation were performed using CNVkit v0.9.6.<sup>64</sup> Segments with copy number  $\geq 4.5$  were extracted as “seed” regions using AmpliconSuite-pipeline (April 2020 update).<sup>65</sup> For each seed, discordant read pairs indicative of genomic structural rearrangement were identified within and up to 50kbp distal the query region. Genomic segments were defined by genomic breakpoint locations (identified by discordant reads) and by modulations in genomic copy number. An assembly graph of the amplicon region was constructed using the CN-aware segments and the genomic breakpoints, and cyclic paths are extracted from the graph. Amplicons were classified as cyclic (ecDNA(+)), breakage-fusion-bridge, complex non-cyclic, linear, or no focal amplification using the heuristic-based companion script AmpliconClassifier. Biosamples with one or more amplicons classified as ecDNA were labelled ecDNA(+), and all others were labelled ecDNA(-).

### **PDGFRA inhibitor testing in patient derived mouse and human in vitro models**

For drug testing, 500 cells per well were plated in 384 well clear bottom tissue culture plates. For seven day assays, cells were treated at 24 and 96 hours post plating with compounds ranging from 10nM to 10 μM manually or using the D300e digital dispenser (HP) and viability was assessed at 7 days following initial drug treatment using the CellTiter-Glo system. For ligand-dependent sensitivity assays, cells were grown in full, growth factor containing media for 24 hours after passaging, and then transferred to media without any growth factors (no PDGA/B, no EGF, no FGF) for overnight starvation. Then, cells were kept in media with regular concentrations of B27 without vitamin A, Heparin, EGF and FGF with one of the following PDGFA/B ligand conditions: No PDGFA/B = 0 ng/ml PDGF AA

and BB each, Low PDGFA/B = 2 ng/ml PDGF AA and BB each, Normal PDGFA/B = 10 ng/ml PDGF AA and BB each, High PDGFA/B = 50 ng/ml PDGF AA and BB each. Cell viability for PPK and 154C was monitored by XTT Cell Proliferation Assay kit (Cayman Chemical) utilizing the included protocol. Absorbance readings were collected using the Synergy HTX Multi-Mode Microplate Reader (BioTek Instruments). Cell viability for all other lines was monitored by CelltiterGlo assay (Promega) and luminescence readings were collected using the Clariostar plate reader (BMG Labtech). IC50 values were obtained using the spline curve model in GraphPad PRISM. All *in vitro* treatments were completed with research-grade dasatinib, avapritinib, axitinib and crenolanib.

### **In vitro kinase inhibition assays**

Dasatinib, avapritinib, axitinib and crenolanib were purchased from Selleck Chemicals. Dimethyl sulfoxide (DMSO) was purchased from Sigma Aldrich. Kinase inhibition assays were performed using Thermo Fisher SelectScreen Kinase Profiling Services. Drugs were sent to Thermo Fisher at concentration of 1 mM in DMSO. The Z'-LYTE assay was performed, which uses a fluorescence-based, coupled-enzyme format to create IC50 curves for inhibitors and kinases per their established protocol.

### **Kinome tree generation**

Kinome illustrations reproduced by the courtesy of Cell Signaling Technology, Inc. ([www.cellsignal.com](http://www.cellsignal.com)). Trees for specific drugs were generated using KinMap (<http://www.kinhub.org/kinmap/>). Data for dasatinib kinome was obtained from Harvard Library of Integrated Network-based Cellular Signatures (LINCS) (<https://lincs.hms.harvard.edu/>). Data for avapritinib was generously shared by Blueprint Medicines.

### **Immunoblots**

For day 3 immunoblot analysis, cells were treated at 24 hours and collected at 96 hours post plating. For day 7 immunoblot analysis, cells were treated at 24 and 96 hours and collected 7 days post plating. Treated cells were lysed in RIPA buffer containing phosphatase and protease inhibitors and immunoblotting was performed. Membranes were probed with primary antibodies overnight: PDGFRA\*, pPDGFRA (Y754)\*, S6, pS6 (S235/236), AKT, pAKT (S473), tubulin. Secondary antibodies were incubated for 1 hour and detected with iBright CL1000 (Invitrogen). Immunoblot results were quantified with area measurements using ImageJ. \*Incubating PDGFRA antibodies required several days.

For immunoblots investigating the downstream signaling in response to ligand stimulation and avapritinib treatment, cells were grown in full, growth factor containing media for 24 hours after passaging, and then transferred to media without any growth factors (no PDGFAA/BB, no EGF, no FGF) for overnight starvation. Then, cells were either kept in media without PDGFAA/BB and without avapritinib, media without avapritinib with PDGFAA/BB (10 ng/mL) for 15 or 60 minutes, or media with avapritinib (1  $\mu$ M) for four hours and with PDGFAA/BB (10 ng/mL) for 15 or 60 minutes. Cell pellets were collected on ice and further processes for immunoblotting as described above.

For immunoblots investigating the degradation and stability of PDGFRA in response to ligand stimulation and avapritinib treatment, cells were grown in full, growth factor containing media for 24 hours after passaging, and then transferred to media without any growth factors (no PDGFAA/BB, no EGF, no FGF) for overnight starvation. Then, cells were either kept in different conditions as indicated, with variable addition of cycloheximide (20  $\mu$ g/ml) for 2 or 4 hours, variable addition of PDGFAA/BB (10 ng/ml each) for 15 min, 60 min, 2 hours or 4 hours and variable addition of avapritinib (1  $\mu$ M) for 2 or 4 hours. Cell pellets were collected on ice and further processes for immunoblotting as described above.

### **PDGFRA flow cytometry**

Cells were seeded in regular tumor stem media overnight. Afterwards, the media was changed to media without PDGFAA/BB (regular B27 without A, Heparin, EGF and FGF). For day 3 flow cytometry analysis, cells were treated with 500 nM avapritinib at 24 hours and collected at 96 hours post plating. For day 7 flow cytometry analysis, cells were treated at 24 and 96 hours and collected 7 days post plating. After collection, cells were dissociated with accutase, washed with PBS and stained with a PDGFRA-APC antibody (Biolegend, clone 16A1, APC conjugated).

### **Immunofluorescence**

Cells were grown as adherent cultures on poly-D-lysine and laminin-coated glass coverslips (R&D systems) and seeded in regular tumor stem media overnight. Afterwards, the media was changed to media without PDGFAA/BB (regular B27 without A, Heparin, EGF and FGF). 24 hours after plating, the cells were treated with 500 nM avapritinib or DMSO and again 72 hours after the first drug-ging. Seven days after treatment, cells were fixed with 4% paraformaldehyde for 15 minutes at room temperature. Cells were washed with PBS and subsequently permeabilized and blocked with 5% normal goat serum (Sigma Aldrich) and 0.2% Triton X-100 in PBS (blocking solution) for 30 minutes at room temperature. The cells were incubated with primary antibodies overnight at 4°C in blocking solution. Primary antibodies used in this study were rabbit anti-PDGFRA (1:500; Cell Signaling Technologies, 3174) and mouse anti-GM130 (1:100; BD Transduction Laboratories, 610822). The following day, the cells were washed with PBS three times, incubated with fluorophore-conjugated secondary antibodies at 1:1000 dilutions (Alexa Fluor 568 goat anti-mouse; Alexa Fluor 488 goat anti-rabbit, Thermo Fisher Scientific) for 1 hour at room temperature, and washed in PBS three more times. Cells were mounted onto SuperFrost Plus microscope slides using ProLong Gold Antifade Mountant with DNA Stain DAPI (Fisher Scientific).

Analysis of immunostaining of treated cells was performed with a 100X oil immersion objective on a laser-scanning confocal microscope (Zeiss LSM 980 with Airyscan 2) operated with the Zen Microscopy Software (Zeiss). All images were processed using ImageJ software (National Institutes of Health).

### Cell cycle and apoptosis assays

Cell lines were treated with 500nM avapritinib at 24 hours and 96 hours and analyzed seven days after first drugging. For cell cycle analysis, cells were incubated with EdU (Click-iT plus EdU Flow Cytometry Kit AF647 (Invitrogen)) 24 hours prior to analysis. Cells were processed following the manufacturer's instructions and stained with Alexa Fluor® 647 azide and FxCycle Violet Stain (Invitrogen). For apoptosis analysis, cells were stained with AnnV PerCP5.5 (Biolegend) and Dapi (Thermofisher). FACS measurements were performed on BD FACSCelesta and analyzed with FlowJo.

### Cell line Nanopore WGS and copy number analysis

For confirmation of *PDGFRA* copy number, QCTB-R059 and GSC-8 cells were grown in TSM or GSC media with or without 1  $\mu$ M avapritinib for 48 hours (acute treatment). Genomic DNA was extracted from R059 cells and control non-tumor human DNA using Qiagen DNeasy Blood and Tissue DNA extraction kit (#69504) according to manufacturer's instructions. Resulting DNA (800-1000ng) was sequenced using Oxford Nanopore Technologies (ONT) MinION sequencer (#SQK-NBD114.24) according to manufacturer instructions. Resulting sequencer output was basecalled using ONT Guppy basecaller (v6.5.7) and aligned to the human reference genome (hg19) using minimap2 (v2.17). To estimate *PDGFRA* copy number increases in R059 and GSC-8 cells, we used BioRad QX200 droplet-digital PCR (ddPCR) system and a BioRad *PDGFRA* copy number estimation assay (#10031240, #10031243). The assay was performed in triplicate and resulting copy numbers were determined in the QuantaSoft software (v1.7.4) by isolating distinct populations of droplets. To estimate copy number, we applied the CoRAL long read copy number analysis toolkit to the aligned WGS data using default parameters. Code is available at: AmpliconSuite/CoRAL: <https://github.com/AmpliconSuite/CoRAL>.

### Orthotopic H3K27M mouse model experiments

For the BT245 orthotopic xenograft model,  $5 \times 10^5$  cells were injected stereotactically into the pons of 6-week old female NSG mice (NOD.Cg-Prkdcscid Il2rgtm1Wjl/SzJ, The Jackson Laboratory). The skull of the mouse was exposed through a small skin incision, and a small burr hole was made using a 25-gauge needle at the selected stereotactic coordinates zeroed on lambda: -2.0 mm X, +1.0 mm Y and 2.5 mm Z. Cells were loaded into a 33-gauge Hamilton syringe, and injected at a rate of 0.5  $\mu$ l/min with use of an infusion pump. Upon completing injection, the needle was left in place for another minute, then withdrawn slowly to help reduce cell reflux. After closing the scalp with suture and staple, mice were returned to their cages placed on a warming pad and visually monitored until full recovery. For the PPK model,  $5 \times 10^5$  cells were injected stereotactically into the pons of 6-week-old female C57BL6/J mice (The Jackson Laboratory). Tumor growth was monitored by bioluminescence (BLI), and avapritinib (Selleckchem, S8553) treatment was initiated 20 days after surgery (PPK). Since BT245 tumors did not show a reliable bioluminescence signal, treatment was initiated empirically at day 98 after injection. For the SU-DIPG XIIP\* orthotopic xenograft model,  $3 \times 10^5$  SU-DIPGXIIIP\* cells stably expressing luciferase were injected stereotactically into the pons of 6-week old female NSG mice (NOD.Cg-Prkdcscid Il2rgtm1Wjl/SzJ, The Jackson Laboratory) and avapritinib treatment was initiated when average cohort bioluminescence signal had reached a threshold of  $1 \times 10^6$ . Avapritinib treatment was performed with 30 mg/kg q.d. for the times indicated in the respective figures. The vehicle used for avapritinib or as a control was 0.5% carboxymethylcellulose (CMC) + 1% Tween-80. Tumor growth was followed with monthly, and upon treatment initiation, weekly, BLI via IVIS Spectrum *In Vivo* Imaging System (PerkinElmer) as described below. Mice were observed for signs of distress and euthanized following development of neurological symptoms (head tilt, seizures, sudden weight loss, ataxia). GraphPadPRISM was used for Kaplan Meier survival analysis. Several PPK and BT245 mice were perfused with 4% paraformaldehyde at moribund status, with avapritinib treatment occurring 1 hour before euthanasia and perfusion, for subsequent immunofluorescence analysis.

### Bioluminescence imaging (BLI)

Tumor growth was monitored monthly, using the IVIS Spectrum *In Vivo* Imaging System (PerkinElmer), starting at 2.5 months post cell injections. Briefly, mice were injected subcutaneously with 75 mg/kg D-luciferin potassium salt (Promega Cat#E1605) in sterile PBS, and anesthetized with 2% isoflurane in medical air. Serial BLI images were acquired using the automated exposure set-up. The peak BLI signal intensity within selected regions of interest (ROI) was quantified using the Living Image Software (PerkinElmer), and expressed as photon flux (p/sec/cm<sup>2</sup>/sr). Representative planar BLI images were displayed with indicated adjusted minimal and maximal thresholds.

### Multiplexed immunofluorescence and image analysis of *in vivo* orthotopic tumor specimens and patient tumor tissue samples

FFPE tissue sections were deparaffinized and rehydrated. Antigen retrieval was performed using a pressure cooker and 1x citrate buffer, pH 6.0. Subsequently, sections were stained using the Opal Polaris 7 Color Manual IHC Detection Kit (Akoya Biosciences). Image analysis was performed by using inForm analysis software (Akoya Biosciences) and the open-source software for digital pathology image analysis QuPath. The following primary antibodies were used at a 1:100 dilution: Recombinant Anti-Histone H3

(mutated K27M) antibody (Abcam, ab190631), Recombinant Anti-PDGFR alpha antibody (Abcam, ab234965), Purified Mouse Anti-Ki-67 Clone B56 (BD, 550609), Human Phospho-PDGFR alpha (Y762) Antibody (RnD Systems AF21141), Phospho-S6 Ribosomal Protein (Ser240/244) (D68F8) XP® Rabbit mAb (Cell Signaling, 5364S), Phospho-Akt (Ser473) (736E11) Rabbit mAb (Cell Signaling, 3787) and EGFR Monoclonal Antibody H11 (Thermo Fisher, MA513070).

### Phosphoproteomics

The relative phosphorylation levels of 49 RTKs were analyzed in fresh frozen samples of human brain tumors using the Human Phospho-RTK Array kit (R&D Systems, Minneapolis, MN, USA), and the relative phosphorylation levels of 39 RTKs were analyzed in mouse samples using the Mouse Phospho-RTK Array kit (R&D Systems, Minneapolis, MN, USA) according to the manufacturer's protocol. The levels of phosphorylation were quantified using ImageJ software. The analysis was performed as previously described.<sup>66</sup>

### C57/BL6J mouse pharmacokinetic analysis

For mouse pharmacokinetic quantification, 6 week old wild type C57BL/6J mice (The Jackson Laboratory) were treated with avapritinib at 30mg/kg orally administered once daily dissolved in 0.5% carboxymethylcellulose carrier. Serum samples were collected at 30 minutes, 6 and 24 hours following a single daily dose. Brain tissue was collected following eight days of daily treatment at 24 hours after administering the 8<sup>th</sup> dose. Frozen tissue samples were homogenized as previously described.<sup>67</sup> Total (free plus protein bound) avapritinib was measured in plasma and tissue homogenates by high performance liquid chromatography with tandem mass spectrometric detection. The lower limit of quantitation was 0.25 ng/mL for determination of the drug in plasma and 1.75 ng/g for tumor tissue.

### CD1 mouse pharmacokinetic analysis

PK analysis accomplished with help of University of Michigan College of Pharmacy pharmacokinetics core. 60mg/kg avapritinib was administered to CD1 mice by oral gavage of avapritinib. At two, four and twenty-four hours after gavage, the mice were isoflurane/oxygen-anesthetized and 500  $\mu$ L to 1 mL of blood was drawn from the apex of the heart within the mouse's enclosed cavity. Immediately, the withdrawn blood was centrifuged within a microvette EDTA coated conical tube for 10 minutes at 10,000 RPM, and the plasma was separated and stored at -80°C until PK analysis was performed. Following the blood draw, the mouse was sacrificed and the brain was extracted separately and stored at -80°C until PK analysis was performed.

### Patient pharmacokinetics

Patient CSF was collected via Ommaya reservoir or during surgical resection. Tissue samples were collected at the time of surgery. Patient CSF pharmacokinetics were analysed with an LC-MS/MS method with an assay range 0.50 to 750 ng/mL for the determination of avapritinib in human CSF using avapritinib as the internal standard (IS). Linearity was  $R^2 \geq 0.9991$ . Avapritinib and the IS were extracted from human CSF using 50:50 DMSO/Acetonitrile (ACN). Plasma was analysed with an LC-MS/MS method with an assay range of 2.00 to 3000 ng/mL for the determination of avapritinib in K2EDTA human plasma using avapritinib as the internal standard (IS). Linearity was  $R^2 \geq 0.9945$ . Avapritinib and the IS were extracted from human plasma using 50:50 DMSO/Acetonitrile (ACN). For both matrix, MS/MS detection was set at mass transitions of  $m/z$  499.3>482.2 for BLU-285 and  $m/z$  507.3>490.2 for avapritinib (IS), in TIS positive mode. Reversed-phase HPLC separation was performed with an X-bridge Shield RP18, 2.1  $\times$  50 mm, 5  $\mu$ m. Mobile Phase A consisted of 0.1% Formic acid and 4mM Ammonium Formate in H<sub>2</sub>O. Mobile Phase B consisted of 0.1% Formic acid and 2 mM ammonium formate in ACN:H<sub>2</sub>O 98:2). LC gradient was run out to 4.5 minutes starting at 35% mobile phase B and ramped up to 100% at 1 minute time mark.

### Neuropsychological assessment

Neuropsychological functions were assessed as per standard of care at the Medical University of Vienna. The testing batteries included WISC V<sup>68</sup> and BASIC-MLT.<sup>69</sup>

### QUANTIFICATION AND STATISTICAL ANALYSIS

Statistical tests were performed using GraphPad Prism 10 or R 4.0.1. For cell and molecular biological methods, statistical analyses are described in detail in figure legends. For statistical comparisons within two groups, we used a two-tailed Student's t-test. Significance values are given in the respective figures.